Adaptive mesh refinement method for the reduction of computational costs while simulating slug flow

J Potgieter[a], L Lombaard[a], J Hannay[b], M A Moghimi[a,c,*], P Valluri[b], J P Meyer[a]

[a] Department of Mechanical and Aeronautical Engineering, University of Pretoria, Pretoria, South Africa

[b] School of Engineering, The University of Edinburgh, Edinburgh, United Kingdom

[c,*] Department of Engineering, Staffordshire University, Stoke-On-Trent, United Kingdom. Email address: Mohammad.Moghimi-Ardekani@staffs.ac.uk

Abstract – Microchannel flow boiling has been the focus of many experimental and numerical investigations due to the high heat transfer coefficients that it can induce. However, experimental research has been limited due to the small scales involved, leading researchers to employ computational fluid dynamics (CFD) simulations to resolve the dearth of research on microchannel flow boiling. Conventional CFD methods use a fine uniform mesh to capture the small scales and gradients, such as the liquid-vapour interface. This method has a large computational cost, and as a result, most research reported in the literature has been limited to two-dimensional axisymmetric domains. An interface-tracking adaptive mesh refinement model was created in this study to overcome the limitation of high computational costs without losing accuracy. This model dynamically refined the mesh only in the regions of interest and allowed a coarser mesh in the rest of the domain. This novel approach was able to recreate previously published results with a maximum error of 6.7%, while using less than 1.6% of the mesh elements. Several simulations were conducted in ANSYS Fluent 19.1 to determine the optimal settings for this new method to maintain accuracy and reduce cell count. These settings were determined as three levels of refinement (δ_L = 3), four refined cells on either side of the interface (δ_M = 4), and was implemented every five time steps (δ_T = 5). Finally, a case study was conducted to illustrate the possibility of simulating two-phase flow in microchannels in three dimensions with this method.

Keywords: *Flow boiling; Microchannel; Adaptive mesh refinement; Computational fluid dynamics*

1. Introduction

Flow boiling is used for thermal management of engineering applications (e.g. electronic cooling and micromixing) because it is more effective than single-phase forced convection. There are different flow regimes present in flow boiling as it develops. The initial regime is bubbly flow, which is characterised by small bubbles. As the bubbles grow and form alternating vapour and liquid slugs, the flow is called slug flow. Then the regime develops further into annular flow as the vapour slugs coalesce. Slug flow, in particular, is of interest due to the presence of recirculating zones in both the liquid and vapour slugs. The recirculation of the fluids enhances the heat transfer and mixing properties of the two-phase mixture. Therefore, it is one of the most investigated flow-boiling regimes [1]. By enhancement in manufacturing technologies, microchannels are widely introduced for various thermal management of engineering technologies [2], and consequently, slug flow in microscale has attracted the attention of researchers [3]. Although technological progress in the field of data capturing has enabled researchers to record the effect of small-scale phenomena on heat and mass transfer more accurately (e.g. via high-resolution infrared cameras in the visualisation of temperature distributions within microchannels), the current technology cannot accurately predict the exact state within the microchannel. In addition, the experimental observations are influenced by various factors such as the size of the channels, the reflective indexes of the channel material and the minuscule time variations. These factors provide a challenge for investigating flow-boiling phenomena. As reported by Szczukiewicz et al. [4], the characteristic times of certain phenomena in flow boiling (e.g. bubble nucleation) are smaller than the response times of most thermocouples.

These restrictions have convinced researchers to use numerical approaches, e.g. computational fluid dynamics (CFD), for modelling small-scale physical phenomena in two-phase flow and gaining valuable insight through numerical modelling. For example, Magnini et al. [5] studied the hydrodynamics and heat transfer of slug flow in an axisymmetric domain and reported that the largest value of the HTC occurred at the minimum thickness of the liquid film, which is generally at the rear of the bubble. The slugs also disturbed the thermal boundary layer in the wake, leaving behind an area with an increased HTC. This was expanded upon by Ferrari et al. [6], who investigated slug flow in a square channel. They found that the slug velocity was higher, and the film thickness was lower than for circular channels due to the fluid moving into the corners of the channel.

Simulating systems of sizes approaching sub-microns and lower is not possible using commercial CFD software due to lack of coupling physical models at these scales. However, for systems of sizes greater than orders 10 μm, errors incurred are quantifiable and can be reduced to manageable levels. These results can be used in combination with experimental results for the development of theoretical models [4]. To properly understand the limitations of commercial CFD software and overcome their challenges in micro-scale modelling, the basic setup steps of CFD must be well understood. To run a CFD simulation, the domain of interest is divided into smaller elements or control volumes, also called cells. During a simulation, the governing equations are solved within each element at every iteration. This leads to a relation between the accuracy of results, the solution time or computational cost, and the number of elements in the solution

domain. To enhance the accuracy of results, the mesh must be refined in the region with high gradients of thermofluid properties; for example, the thin liquid film at the wall of a microchannel [1], bubble formation in two-phase flow [7] and capturing boundary layer in the computational domain [5]. Ensuring the existence of enough mesh resolutions in the regions of the domain where small-scale phenomena take place becomes more challenging, in particular in dealing with transient fluid flow because the region of interest can move around the domain. Therefore, to get accurate solutions in the domain, conventionally, researchers used a very fine uniform mesh in the entire computational domain. This approach assured researchers that they always had sufficient mesh resolution across the domain regardless of the location of interested thermofluidic phenomena, for example the bubble formation and bubble interaction in transient flow in a microchannel (see Table 1).

Table 1: List of slug flow studies.

Author	Channel size	Channel shape	Element size & type	Number of mesh elements	2D/3D
Magnini and Thome [3]	0.5 x 22.5 mm	Axisymmetric	D/300 Uniform Structured	2 000 000	2D
Magnini et al. [5]	1 x 8 mm	Axisymmetric	D/300 Uniform Structured	360 000	2D
Ferrari et al. [6]	0.5 x10 mm	Axisymmetric	D/300 Uniform Structured	900 000	2D
	0.1 x 0.1 x 3-5 mm	Square	D_{eq}/125 Inflation layers at the walls Structured	4.7 - 7.9 $\times 10^6$ (for a quarter of the domain)	3D
Magnini et al. [8]	0.5 x 10-36 mm	Axisymmetric	D/300 Uniform Structured	0.9 - 3.24 $\times 10^6$	2D
Gupta et al. [9]	0.5 x 5 mm	Axisymmetric	D/100 Inflation layers at the walls Structured	53 000	2D
Liu et al. [10]	0.3 x 0.3 x 12 mm & 0.3 x 0.3 x 2.1 mm	Square T-section	D/15 Uniform Structured	392 000	3D

On the other hand, using a uniform refined mesh increases the number of cells in the domain, which means the computational cost of the simulation increases significantly since governing equations must be solved for each cell. The approach of using a uniform and very fine mesh across a domain might seem inevitable, especially in modelling flow boiling in microchannels because the minute scales of the phenomena existing in the domain require very fine spatial mesh elements to capture the fluid flow characteristics accurately. Due to the transient nature of the flow, the required time steps should be defined very small to have stable numerical solutions. These factors, namely the small spatial elements and temporal time steps, lead to high computational costs of microchannel flow-boiling modelling, resulting in most studies being limited to 2D axisymmetric assumptions (see Table 1).

Therefore, the question is whether it is possible to significantly reduce the computational cost with no penalty on result accuracy in the modelling of microchannel slug flow. Answering this question depends on what physical model is available for slug flow. One of the most-used models for investigating slug flow was developed by Thome [11]. This model attempts to simulate heat transfer during slug flow while the bubbles move past the area of interest. For this model, the microchannel is divided into three regimes, each with its own heat transfer coefficient (HTC). First, a liquid slug flows over the area of interest, followed by an evaporating elongated bubble, and finally, a vapour slug. It is assumed that numerous bubbles will start to nucleate on the microchannel wall. The bubbles only detach and join the bulk flow after their radii have grown and reached the other walls. Then they continue to grow in the axial direction; the flow is then in the slug regime with alternating vapour and liquid slugs [1]. In the numerical modelling of slug flow; it is vital to have a very fine mesh in the region of interest (in the vicinity of bubble region in the domain), while in the bulk flow region, which no longer contains small-scale phenomena, the mesh element can be significantly coarse. This adaptive mesh idea has been implemented by some researchers in two-phase flow. For example, Mehdizadeh et al. [12] recreated a previous study on slug flow with a 96% reduction of cells by implementing adaptive mesh refinement. Their study was based on a uniform 2D axisymmetric mesh with a base cell size of 50 µm. The cells around the interface were refined eight times, achieving a size of 6.25 µm. The adaption metric was the gradient of the volume fraction, and refinement was applied every five time steps to cells with a value above 0.1. Fondelli et al. [13] used a similar method on a macroscale model, allowing for larger cells. A dam-break problem was replicated in 3D, proving that mesh adaption can be used in 2D and 3D studies. Zhou and Ai [14] studied mesh adaption for moving immersed boundaries. The cases they studied included a swimming fish and vortex shedding. By reducing the number of nodes of the swimming fish model from 749 724 to 60 410, they reported that the adaptive mesh had a solution time of one-tenth that of the uniform mesh. Bayareh et al. [15] further reported that implementing an adaptive mesh reduces the computational time.

Therefore, this study emphasised the use of an adaptive mesh refinement model in numerical modelling of flow boiling to provide not only an accurate solution but also a significant reduction in computational efforts. To enhance the adaptive mesh refinement effect in microscale boiling, a smeared source term-based mass transfer model was considered to conserve the net mass transfer across the interface. However, it would limit the vapour and liquid source terms to the pure vapour and liquid domains respectively. The physical

features of two-phase flow would be captured by proper recognition of the vapour-liquid interface and refining mesh over the region, while in the rest of the domain, even with a coarse mesh, the simulation could provide accurate results because it would deal with single-phase flow (either liquid or vapour phase). This approach would save significant computational effort with a negligible penalty in result accuracy. Since the proposed model used in this study was not available in commercial software, a series of UDF (user-defined functions) was coded to implement the proposed models. The advantages of the discussed technique will pave the way for future researchers to get the results of flow boiling with minimum effort and to run 3D simulations of flow boiling with conventional computer resources.

Other aspects of microchannel heat sinks that have been studied are internal pins or fins and the orientation of the channel. While many studies have investigated various internal fins and pins [16-18], only a few orientations have been investigated. The change of the orientation of the microchannel can be described as rotated or inclined. When rotated, the flow direction remains constant and the channel is rotated around the flow. For an inclined channel, the flow direction is rotated and the vector component of gravity parallel to the flow changes. While rotational orientation has been investigated at several different positions by researchers such as Ajith Krishnan et al. [19] and Vermaak et al. [20], inclined orientation is limited to flow that is either perpendicular or parallel to gravity [21, 22], resulting in an area of research that needs to get more attention.

This study starts with a quick overview of the domain configuration. A discussion of governing equations follows, and the proposed method for adaptive mesh strategy is discussed. Then the proposed method is verified against the literature, and finally, the presentation follows of several simulations conducted on various adaptive refinement aspects, including the refinement level, the refinement area and the refinement frequency to conclude the developed model by demonstrating its advantages and disadvantages, such as the reduction in the required cell count of the model and some of the model's limitations. Finally, a case study using the developed mesh refinement method is presented.

2. Numerical methodology

2.1. Computational domain

To investigate the impact of adaptive mesh refinement on the reduction of the computational cost, which is extremely high in simulating the microscale phenomena, this study investigated the interaction between two fluid phases in a microchannel. The study considered the refrigerant R113 phases (liquid and vapour) as working fluid where the phases were incompressible, immiscible, viscous and Newtonian flowing within a 2D laminar microchannel. The domain consisted of an axisymmetric microchannel of width D = 0.5 mm and length 20 D, which is shown in Figure 1, as used in the experiments of Vermaak et al. [20]. A pill-shaped bubble was patched into the domain at the inlet of the channel, which had an initial adiabatic region that was 8 D in length, followed by a heated region that was 12 D in length. A uniform mass flux of 600 kg/m^2 was set at the inlet, and a zero-gauge pressure outlet condition was maintained. The fluid entered the domain at saturation temperature, which was 323.15 K. A heat flux of 9 kW/m^2 was applied to the heated surface, and

a no-slip condition was set at the walls. The initial location of the bubble and the boundary conditions are displayed in Figure 1.
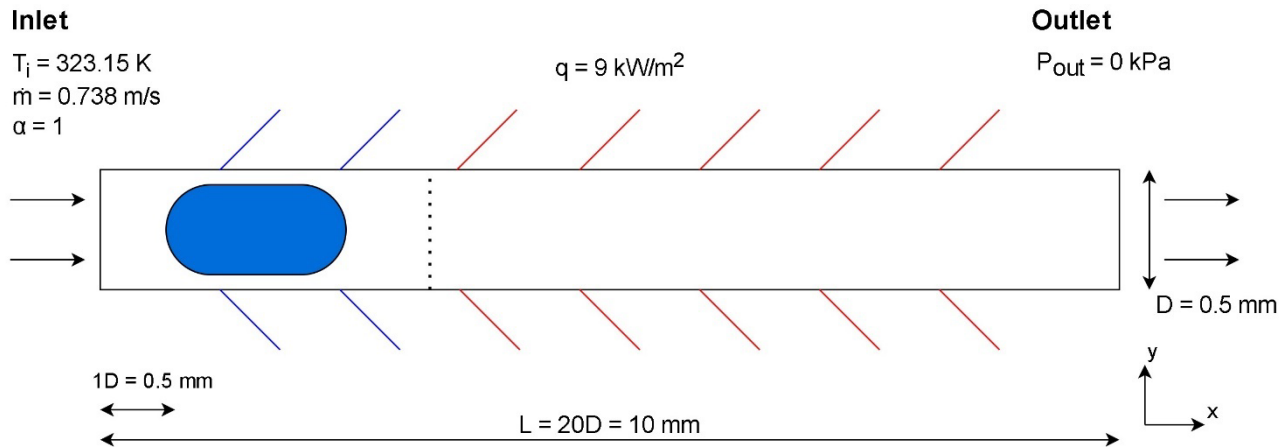

Figure 1: Bubble location and boundary conditions (not drawn to scale)

Table 2: Properties of R113 (adapted from Ferrari et al. [6]).

Property	Dimensions	Value
Liquid density	kg/m^3	1 502
Vapour density	kg/m^3	8
Liquid viscosity	μPa.s	477
Vapour viscosity	μPa.s	10.4
Liquid-specific heat	J/kg.K	943
Vapour-specific heat	J/kg.K	695
Liquid conductivity	mW/m.K	63.2
Vapour conductivity	mW/m.K	9.62
Saturation temperature	K	323.15
Surface tension	N/m	14.4
Latent heat capacity	kJ/kg	143.5

The two fluids are the liquid and vapour phases of refrigerant R113 (Table 2). These two fluids were represented in the domain as a single fluid via the volume of fluid (VOF) method. The VOF method implemented the single-fluid approach by using a volume fraction, α, which had a value of 1 in the pure liquid region and a value of 0 in the pure vapour region. The interface between the two fluids was modelled as a smearing of the volume fraction, which rapidly changed from 0 to 1 over a three- to four-cell region. The single-fluid properties, such as density, viscosity and conductivity, were then expressed as a function of the volume fraction via:

$$\emptyset = \emptyset_L c + (1 - c)\emptyset_v \tag{1}$$

where $\emptyset$ is any scalar property and the subscripts L and v represent the liquid and vapour properties respectively.

2.2. Governing equations

During each iteration of the simulation, a full set of idealised Navier-Stokes equations were solved. The following equations are for mass, momentum and energy conservation, scalar transport and volume fraction advection:

$$\nabla(\tilde{u}) = 0 \tag{2}$$

$$\rho\left(\frac{\partial \tilde{u}}{\partial \tilde{t}} + \tilde{u}.\widetilde{\nabla}\tilde{u}\right) = -\widetilde{\nabla}P + \mu\widetilde{\nabla}^2\tilde{u} + \sigma\tilde{\kappa}\tilde{n}\delta \tag{3}$$

$$\rho c_p\left(\frac{\partial T}{\partial t} + \tilde{u}.\widetilde{\nabla}T\right) = \bar{k}\widetilde{\nabla}^2 T + \widetilde{\nabla}h_{fg}\dot{m} \tag{4}$$

$$\frac{\partial \emptyset}{\partial t} + \nabla.\emptyset\tilde{u} = \emptyset\nabla.\emptyset \tag{5}$$

$$\frac{1}{\rho}\left[\frac{\partial}{\partial t}(c\rho) + \nabla.(c\rho\tilde{u})\right] = \frac{1}{\rho}[S_c + S_{mV} - S_{mL}] \tag{6}$$

where ρ is the density (kg/m³), u is the velocity (m/s), P is the pressure (kPa), T is the temperature (K), σ is the surface tension coefficient (N/m), μ is the viscosity (μPa.s), h_L is the latent heat capacity (kJ/kg), $\dot{m}$ is the volumetric mass transfer rate (kg/m³.s), and S is a volumetric source term.

2.3. Solution procedure

Several different methods were required to solve the governing equations at each time step. The solver used throughout the study was pressure-based, with the pressure calculated using the PRESTO! (PREssure STaggered Option), which is a discrete continuity balance. The velocity and pressure were coupled via the PISO (Pressure-Implicit with Splitting of Operators) method. A second-order upwind method was used to calculate the gradients for the energy and momentum equations, and a second-order implicit method was used for the volume fraction. The propagation and reconstruction of the interface were conducted by the compressive scheme, which recreated the interface from the cell values and normal unit that were associated with the cell and its surroundings.

Time advancement was conducted implicitly via a first-order time-stepping method. The time advancement was iterative and solved the continuity, momentum, energy, volume fraction and other scalar equations simultaneously until they had all converged below 1e-6. The time step was calculated via a limited Courant-Friedrichs Lewy number (CFL) criterion, where the time step was found by means of the following [23]:

$$CFL = \frac{u\Delta t}{\Delta x} \hspace{4cm} (7)$$

The time step limitation, which was set to CFL = 0.25, ensured that the distance information travelling during each time step, which is usually carried by the movement of the fluid, did not exceed the characteristic length of the mesh elements. This limitation ensured that the solution remained stable, and an additional limitation of Δt_{max} < 1e-6 s ensured that no more than 1% of the liquid evaporated from each cell within a time step. These limitations produced time steps between 2e-7 s and 1e-6 s for all simulations.

To create fully developed velocity, pressure and temperature profiles within the domain, a steady-state case was run only utilising liquid R113. Once these profiles were present, the domain was changed to a transient domain, at which state a vapour slug was patched near the inlet. The properties of the liquid slug were then set to those at saturation temperature, with uniform pressure, velocity and temperature profiles implemented. Once the vapour bubble had been created, and the domain properties were correct, a transient solution was obtained employing a user-defined function (UDF) to implement mass transfer, which is elaborated on in Section 2.4.

After the bubble had been patched and the liquid-vapour interface was recognised, a UDF was used to implement the mass transfer model as a macroscale model, which focused on evaporation on the interface. The implemented model is discussed in more detail in Section 2.4. The required model was a necessary step for the adaptive mesh approach, as in ANSYS 19.1, there was no two-phase model available to focus on evaporation only at the interface. The UDF then reset the domain mesh to a uniform mesh size in the entire domain and implemented the refined mesh only on a few cells around the liquid-vapour interface due to the smeared mass transfer approach, which was considered in the UDF (discussed in more detail in Section 2.4). The proper implementation of the smeared mass transfer source term would let the proposed adaptive mesh create a coarse mesh within the computational regions where single phases flow (either vapour or liquid), only creating a very fine mesh on the neighbouring cells of liquid-vapour interface where the evaporation phenomenon would take place. The advantage of this method is that it significantly saves computational effort with minimum or no penalty on result accuracy.

The steps that were followed during each iteration of the calculation are shown in Figure 2.
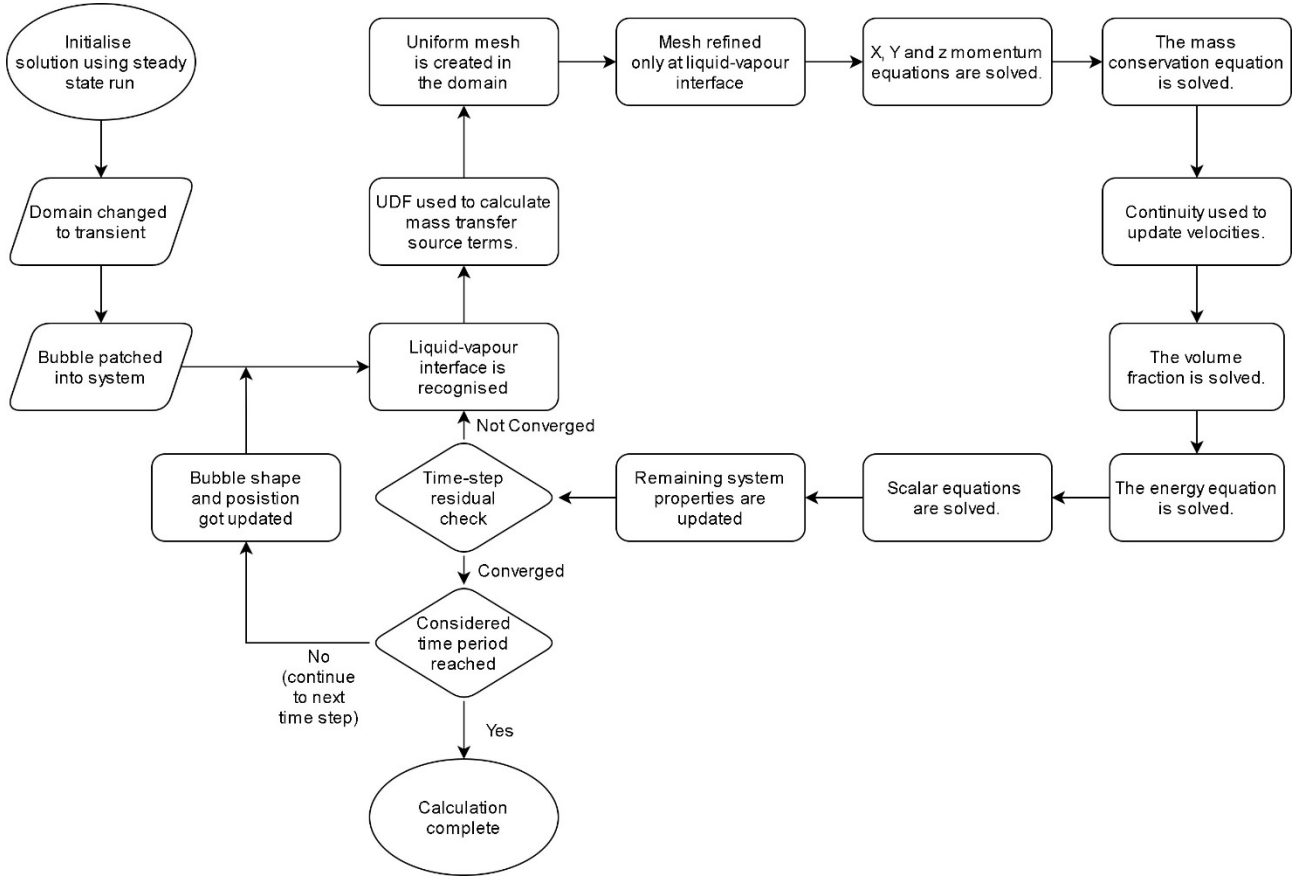
Initialise solution using steady state run

Domain changed to transient

Bubble patched into system

Uniform mesh is created in the domain

Mesh refined only at liquid-vapour interface

X, Y and z momentum equations are solved.

The mass conservation equation is solved.

Continuity used to update velocities.

UDF used to calculate mass transfer source terms.

Liquid-vapour interface is recognised

The volume fraction is solved.

The energy equation is solved.

Scalar equations are solved.

Remaining system properties are updated

Time-step residual check

Not Converged

Converged

Bubble shape and posistion got updated

Considered time period reached

No (continue to next time step)

Yes

Calculation complete

Figure 2: Solution steps through adaptive mesh refinement

2.4. Mass transfer

To focus the evaporation at the interface, the Schrage model was chosen as the basis for the mass transfer model. Many previous studies, such as those by Ferrari et al. [6], Liu and Palm [24] and Magnini and Thome [3], used a variation of this model and all reported a similar phenomenon, namely that mass transfer within the interfacial region caused instabilities with the advection of the volume fraction or the level-set method.

The Schrage model was first proposed by Schrage [25], but the version that was used in this study was simplified by Tanasawa [26]. It was then used to generate the source term-based model by Hardt and Wondra [27]. The Schrage model is based on the kinetic theory of gases and relates the transfer of mass to the difference in partial pressure across the interface, as well as an accommodation coefficient, ω, which is the ratio of excited molecules that cross the interface to the total number of excited molecules that strike the interface. The mass flux is given by:

$$\dot{m} = \frac{2\omega}{2 - \omega} \sqrt{\frac{M}{2\pi R}} \left[\frac{P_g}{\sqrt{T_{g,sat}}} - \frac{P_L}{\sqrt{T_{L,sat}}} \right] \tag{8}$$

where ṁ is the mass transfer rate (kg/m³.s), M is the molecular mass (kg/mol), R_g is a gas constant and $\omega = 1$.

Tanasawa [26] then simplified this equation by assuming that the mass flux across the interface is linearly dependent on the temperature difference across the interface and that $T_{g,sat}$ and $T_{L,sat}$ are both constant and equal. This mass flux was then found using:

$$\dot{m} = \frac{2\omega}{2-\omega}\sqrt{\frac{M}{2\pi R}}\left[\frac{\rho_g h_L(T - T_{sat})}{T}\right]$$
(9)

Once the mass flux was obtained, the mass transfer or source term was calculated as a function of the interfacial area:

$$S_g = -S_L = \dot{m}|\nabla\alpha|$$
(10)

where S_g and S_L are the mass source terms for the vapour and liquid phases respectively.

The interfacial area term in Equation 10 is the magnitude of the gradient of the volume fraction, which ensures that evaporation only happens at the interface. In microscale flows, the tiny cell size focuses the mass transfer to a very small area, which can attempt to evaporate more liquid than which exists in the cell and produce negative volume fractions.

This can interfere with the volume fraction advection equation, which makes the Tanasawa [26] model, in its original form, inappropriate for microscale flow boiling [28]. To better suit the model to microscale boiling, Hardt and Wondra [27] proposed a smeared source term model that would conserve the net mass transfer across the interface but would limit the vapour and liquid source terms to the pure vapour and liquid domains respectively. The location of the implemented source terms is shown in Figure 3.
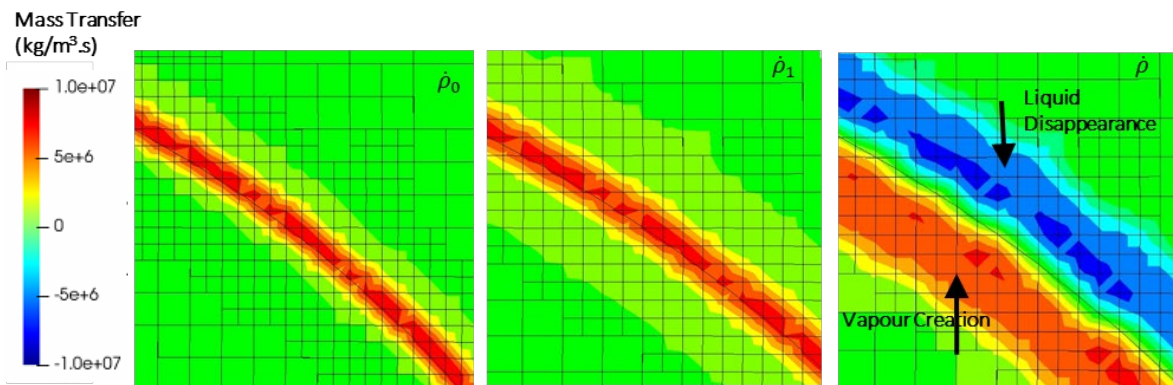
Figure 3: Mass transfer model with an initial source term (left), smeared source term (middle) and implemented source term (right)

The smeared source terms are displayed in Figure 3, and the procedure for implementing the model is as follows:

1. The initial source term, which is shown in Figure 3 (left), was calculated using:

$$\dot{\rho}_0 = N_{to}\dot{m}\alpha|\nabla\alpha| \qquad (11)$$

where $\dot{m}$ is the mass transfer rate, which was found using Equation 9 and where N_t is a normalisation factor, accounting for the shifting of the source term more to the liquid side of the interface caused by the presence of α in the equation.

N_t was calculated using:

$$N_{to} = \frac{\int_V |\nabla\alpha| dV}{\int_V \alpha|\nabla\alpha| dV} \qquad (12)$$

2. $\dot{\rho}_0$, which only existed within the interface, was then smeared over three to four cells on either side of the interface. A steady diffusion equation was used to smear the initial source term, which is shown in Equation 13:

$$\dot{\rho}_1 = \dot{\rho}_0 + D\nabla^2\dot{\rho}_1 \qquad (13)$$

Each boundary had Neumann boundary conditions, ensuring that the integral of the initial and smeared source terms were always equal. The smeared source term is shown in Figure 3 (middle).

3. The smeared source term was then bounded on either side and as well as within the interface. Cells that had a volume fraction of between 0 and 1 were set to 0. The final source term that is shown in Figure 3 (right) and was implemented in Ansys Fluent is as follows:

$$\dot{\rho} = \begin{cases} N_v(1-\alpha)\dot{\rho}_1 & if\ \alpha < 0.001 \\ N_L\alpha\dot{\rho}_1 & if\ \alpha > 0.999 \\ 0 & if\ 0.001 \leq \alpha \leq 0.999 \end{cases} \qquad (14)$$

where N_v and N_L are normalisation factors, which accounted for the bounding of the smeared source term and ensured that the magnitudes of the source terms remained constant.

The vapour and liquid normalisation factors were found using:

$$N_v = \frac{\int_{V_v} \dot{\rho}_0 dV_v}{\int_V (1-\alpha)\dot{\rho}_1 dV} \qquad (15)$$

$$N_L = \frac{\int_{V_L} \dot{\rho}_0 dV_L}{\int_V \alpha\dot{\rho}_1 dV} \qquad (16)$$

where N_v and N_L are the vapour and liquid phases respectively.

4. When mass was moved from the liquid to the vapour domain, the total enthalpy remained constant, which resulted in cooling of the vapour and heating of the liquid. To account for this, as well as the enthalpy of formation, a source term was implemented in the energy equation, as follows:

$$\dot{h} = -\dot{\rho}_0 h_L + N_v(1-\alpha)\dot{\rho}c_{p,v}T - N_L\alpha\dot{\rho}c_{p,L}T \tag{17}$$

The first term accounts for the enthalpy of formation, while the second and third terms are for the vapour and liquid source terms respectively. The mass transfer model was implemented via a UDF, and the steps that were followed are shown in Figure 4.
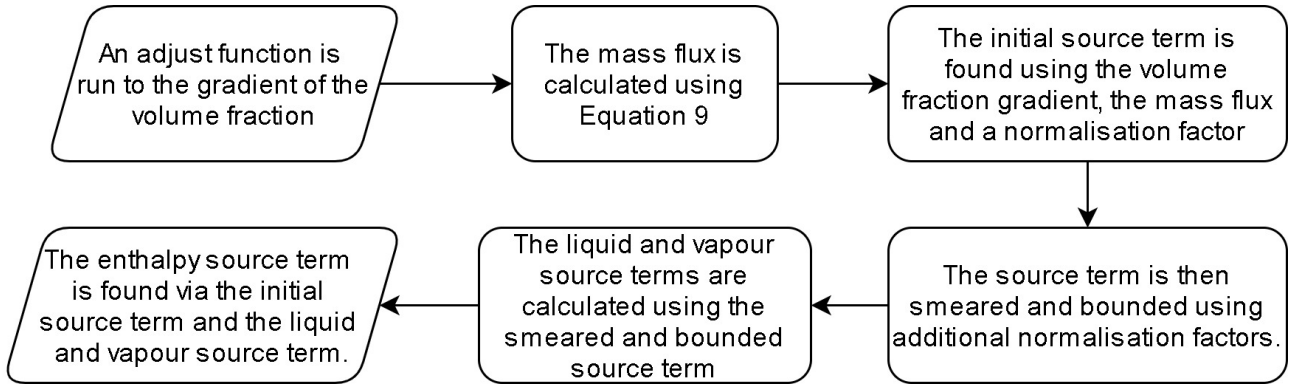
Figure 4: Mass transfer model steps

3. Verification and validation

To ensure that the implemented methods, models and meshing schemes provided accurate results, a series of verification and validation simulations were conducted. The first set of simulations was designed to ensure that the mesh density was high enough to capture the small-scale phenomena that were simulated; the most important of which were surface tension and mass transfer.

The first set of simulations was designed to test the effect of reducing the size of the cells on the solution. Each case had uniform cells within the bulk region, with five layers of inflation applied to the boundaries. Bulk cell sizes of 50, 37.5, 25 and 17 μm were used. The edge cell sizes were 12, 9, 6 and 4 at the boundaries respectively. An adaptive mesh refinement model was used, which refined cells on either side of the liquid-vapour interface. The model implemented three levels of refinement, with a minimum of four refined cells on either side of the interface. The adaption method occurred every five time steps. These parameters are further investigated in the results section.

Each simulation was run for a total of 12.5 ms, at which stage, the vapour slug should have grown to roughly three times its original size and should have almost reached the outlet of the channel. This process is demonstrated in Figure 5, which shows the temperature profile within the channel as well as the location of the bubble, which is outlined in white.
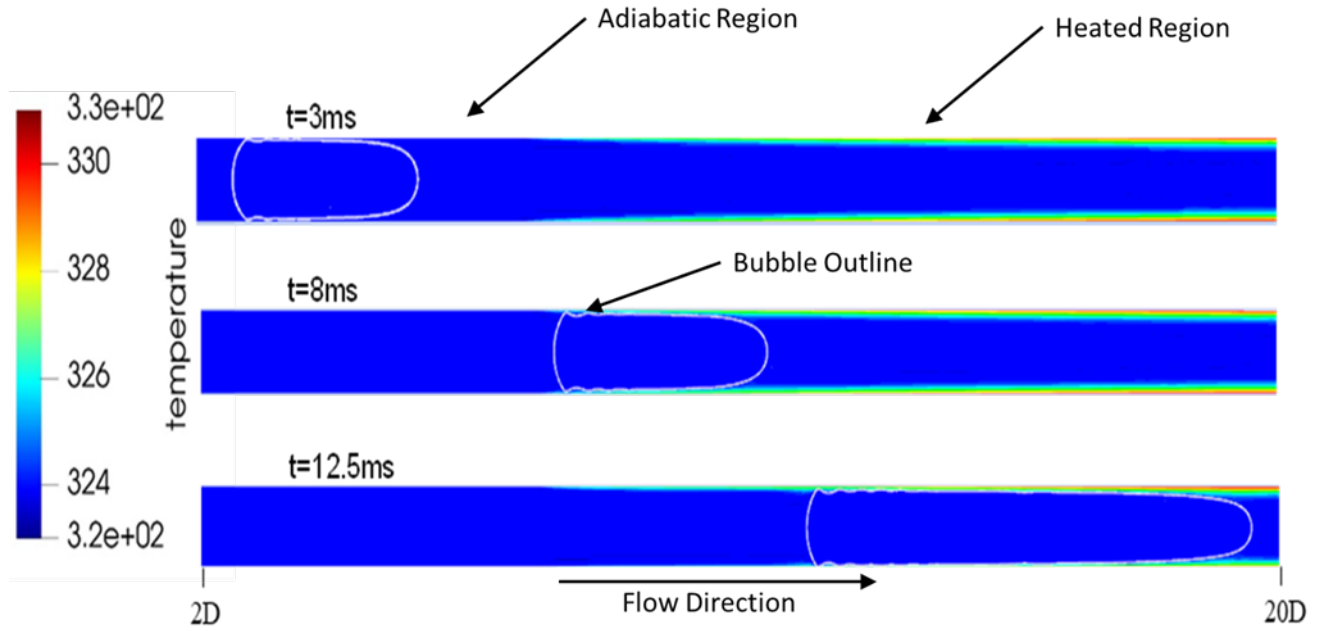
Figure 5: Temperature profile and position of the bubble (white outline) at various times (K)

The results which are compared are the local heat transfer coefficient at the heated surface at the end of the simulation and the dimensionless location of the front and the rear of the bubble throughout the equation. The heat transfer coefficient was calculated using:

$$h = \frac{\dot{q}}{T_{s,c} - T_{sat}} \tag{18}$$

where h is the local heat transfer coefficient (kW/m²K).

The resulting heat transfer coefficients obtained using different element sizes are displayed in Figure 6.
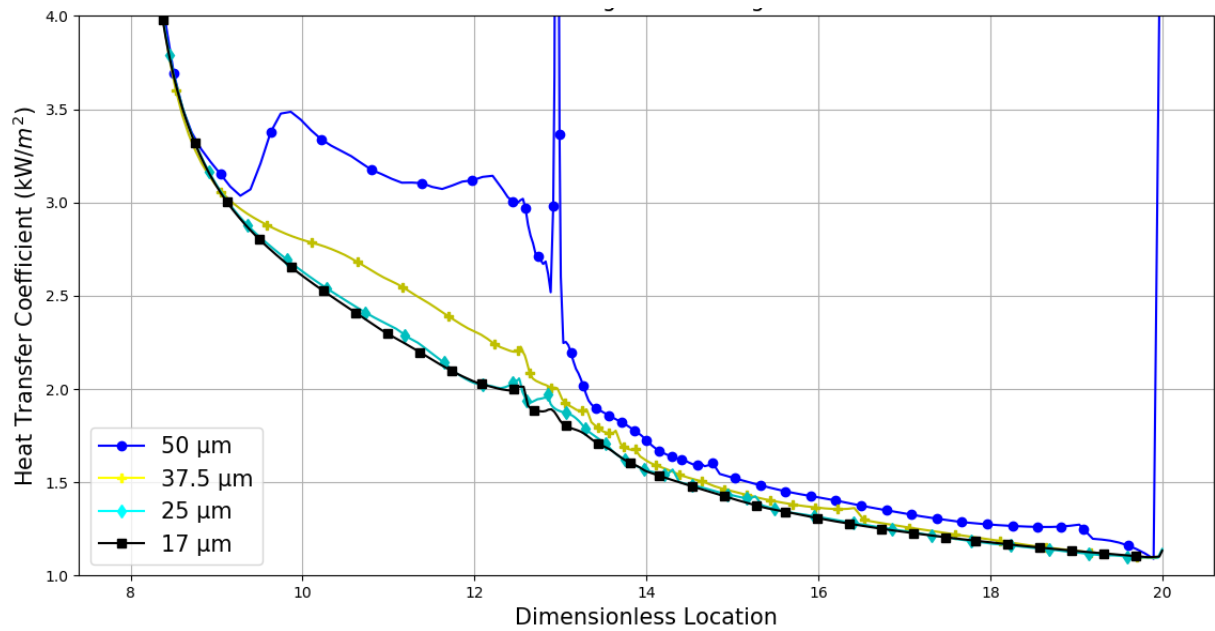
Figure 6: Heat transfer coefficient along the heated surface for different mesh sizes throughout the domain

The case with the largest error was the 50 μm case, which produced uncharacteristic spikes in the heat transfer coefficient. The 37.5 μm case performed better; however, a large difference still occurred once the cell size was reduced. Once the cell size was reduced from 25 μm to 17 μm, there was very little difference between the solutions, with the maximum difference between the two being 4%.
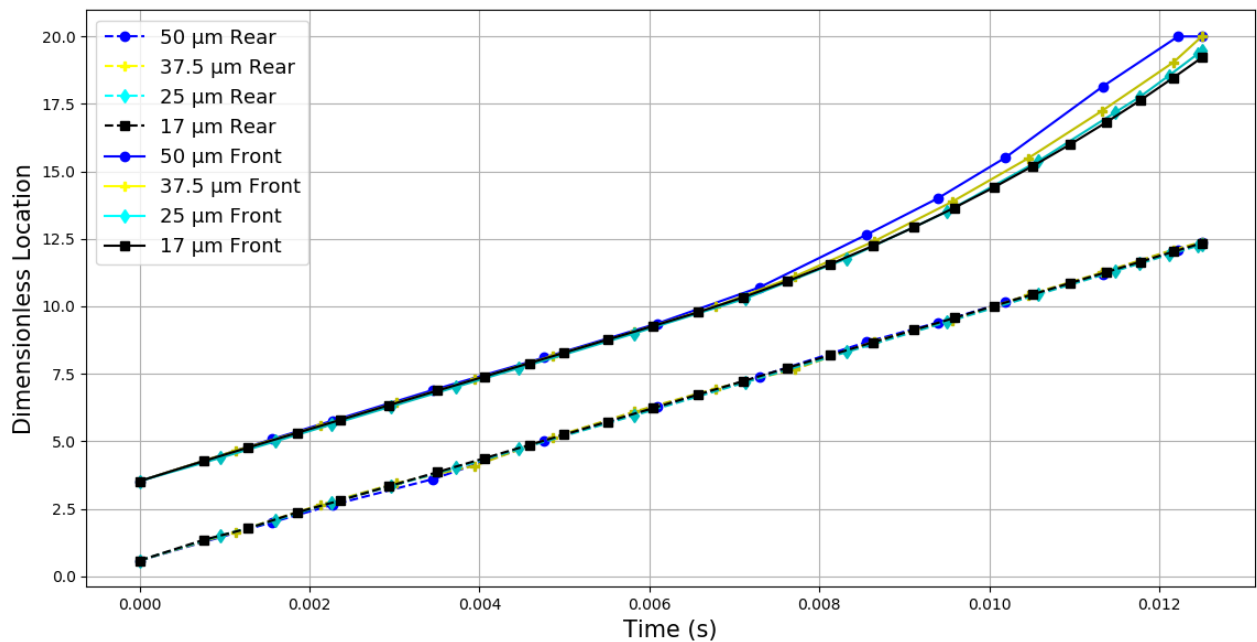
Figure 7: Dimensionless axial position of the front and back of the bubble versus time for different mesh sizes

The results shown in Figure 6 are closely matched by the location of the bubbles, shown in Figure 7. Both the 50 µm and the 37.5 µm case overpredicted the front of the bubble, while the 25 µm and 17 µm cases produced similar results with a maximum error of 1.5%. The rear positions of the bubbles were almost identical, showing that the flow characteristics were correctly represented, with the source of the error coming from the surface tension and the mass transfer.

To visualise the effect of shrinking of the cell size on the solution, the location of the front of the bubbles at 12 ms is plotted in Figure 8. The cells sizes produced the following total cells; 5 500 cells for 50 µm, 9 000 cells for 37.5 µm, 14 000 cells for 25 µm and 28 000 cells for 17 µm. This shows a quick reduction in error as the cell count was initially increased; however, as the cell count was doubled from 14 000 cells to 28 000, the decrease in error was tiny, implying that increasing the cell count would not increase the accuracy of the solution. These results, shown in Figure 6, Figure 7 and Figure 8, led to the conclusion that a bulk cell size of 25 µm was suitable for the following investigation.
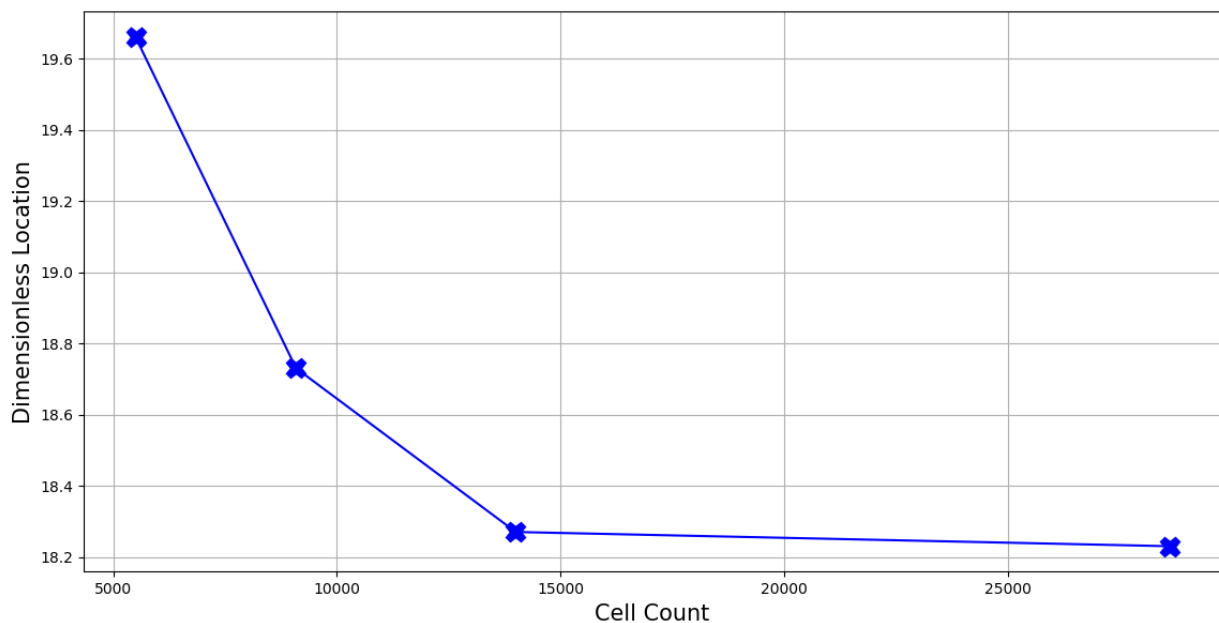
Figure 8: Dimensionless position versus cell count

Even with a mesh that correctly captured the various phenomena under investigation, the different models and methods that were implemented could cause a numerical error. To ensure that the phenomena were correctly represented and calculated, the results of the 25 µm case were compared with previously published research, which was conducted on the same numerical domain with the same working fluid. The same results as before were analysed, namely the HTC at the end of the simulation as well as the dimensionless positions of the bubbles. These studies did not use mesh refinement and required 3.6 to 9 $\times 10^5$ cells, which is over 25 to 60 times the number of cells that were used in this study.

The HTC produced in this study, shown in Figure 9, is sufficiently close to those produced by the two previous studies, with maximum errors between the results being 6.7% for Ferrari et al. [6] and 5.4% for Magnini et al. [5]. The HTC that was obtained when running a steady-state, single-phase simulation is also

displayed in Figure 9. This shows the influence of two-phase flow on the heat transfer characteristics of the microchannel.
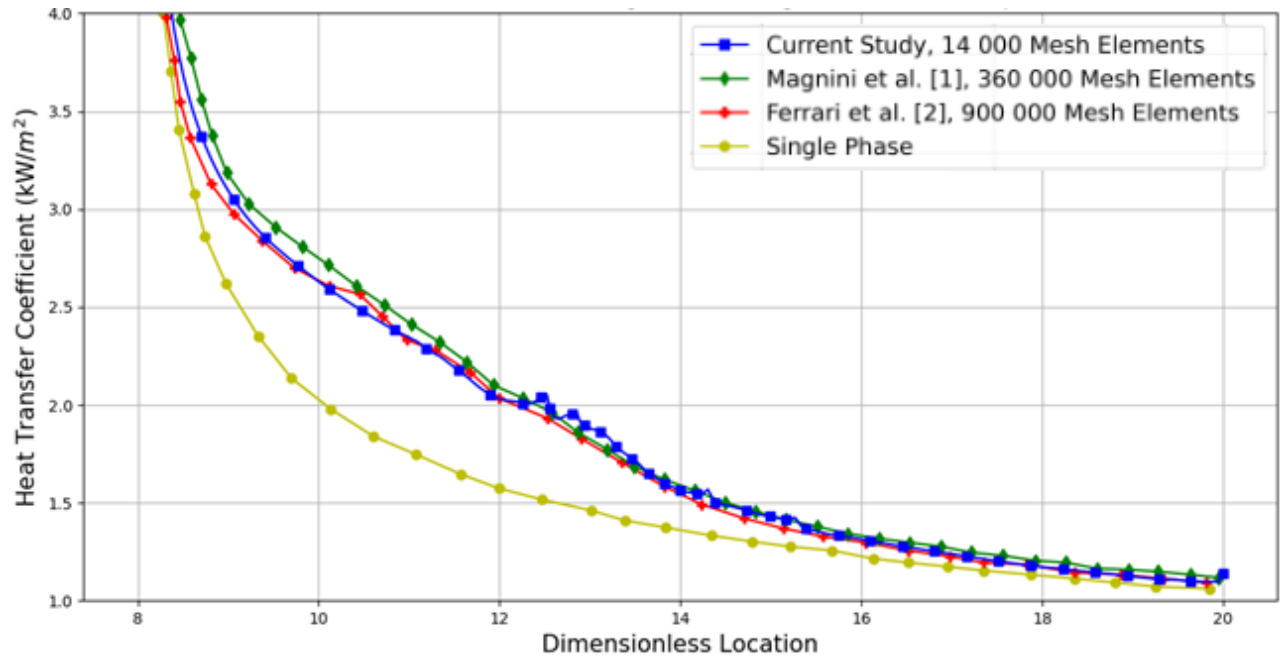

Figure 9: Heat transfer coefficient along the heated surface compared with that of previous numerical studies

The results shown in Figure 10 mimic those shown in Figure 9, with negligible differences between the three cases. The maximum error between this study and that of Ferrari et al. [6] is 2.5%, and Magnini et al. [5] is 3%.
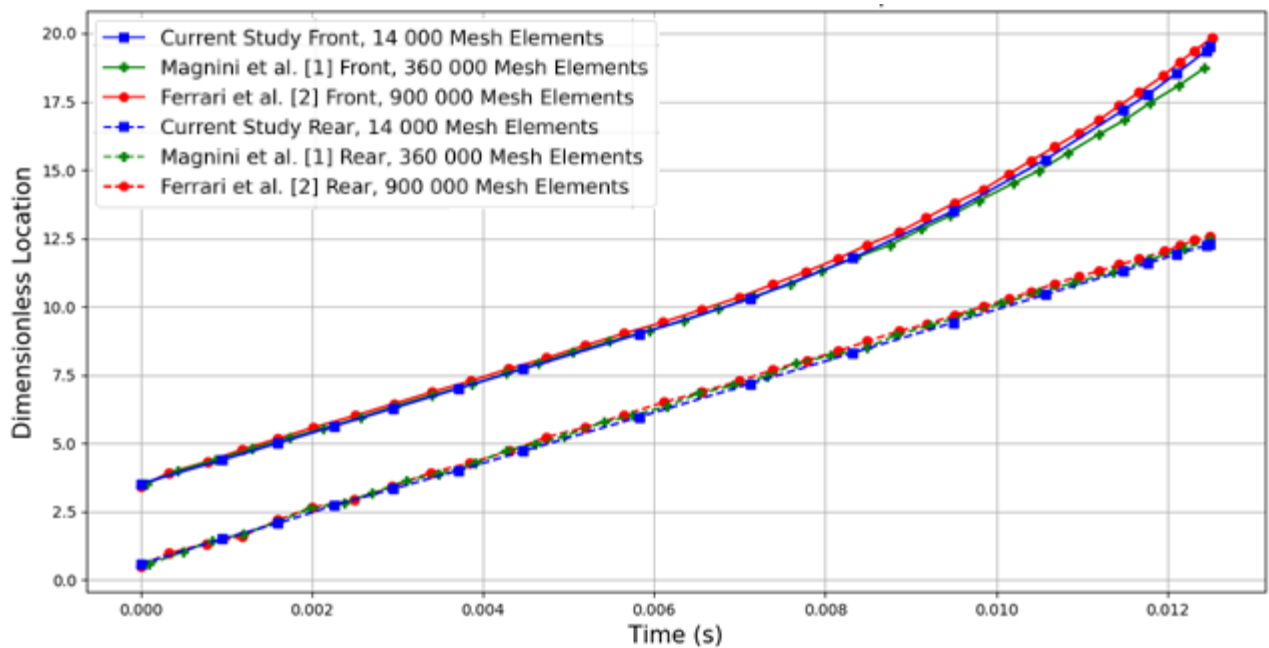

Figure 10: Dimensionless axial location versus time compared with that of previous numerical studies

The results presented in this section proved that the solutions obtained using a mesh with 25 μm bulk cell sizes and the various models and methods were accurate and verifiable against previously published research. Therefore, the question is to what extent can the computational effort of this study be reduced with no penalty on the accuracy of the results. In this regard, the investigation into the effect of adaptive mesh and its corresponding settings is presented in the next section.

4. Results

4.1. Adaptive mesh refinement model

To increase the resolution around specific areas, adaptive mesh refinement can be done. This method changes specific areas of the mesh at set intervals, either every couple of iterations or every couple of time steps. The adaption method is based on the error that is expected to occur over the cell size and the gradient of the specific area. The expected 2D error was calculated via the equation:

$$|e_{i1}| = (A_{cell})^{\frac{r}{2}}|\nabla f| \tag{19}$$

where e is the associated error, A_{cell} is the area of the cell, r is the gradient volume weight, and ∇f is the Euclidean norm of the gradient of the chosen metric.

The purpose of adaptive meshing is to reduce the expected error. Equation 19 indicates that the variables determining the error are the cell area and the gradient. The gradient cannot be changed without affecting the solution. Therefore, reducing the cell area is the best way to reduce the expected error. The default adaption procedure in Ansys Fluent can be based on several different parameters, such as pressure or temperature, but for two-phase flow simulations, the more common parameter is the gradient of the volume fraction, which refines cells that are within the interface. This method was used, for example, by Fondelli et al. [13].

Because of the spurious currents surrounding the bubble interface, which are characteristic of numerical investigations into flow boiling in microchannels, only refining the cells at the interface would not properly capture the mass transfer, temperature and velocity gradients. The mass transfer that was implemented was also smeared over three to four cells on either side of the interface. It was imperative for this study that mass transfer only occurred within refined cells. Therefore, it was necessary to refine a set region on either side of the interface, ensuring that these gradients and mass transfer were captured and that the thin liquid film between the bubble and the wall was fully refined.

To ensure that the cells around the interface are fine enough to capture the solution and that refined cells that are no longer in close proximity to the interface do not induce high computational costs, an execution command is used to implement the refinement at a set frequency. The method implemented in this study was a UDF to create a region around the interface that was refined to consistently have a set minimum number of cells on either side of the interface. Equation 13, which was previously used to smear the mass transfer source

term, was instead used to smear a scalar that was equal to the gradient of the volume fraction. Once it was smeared, it was bounded, and all cells that were within the bounded area were refined. This ensured that the spurious currents existing around the bubbles, as well as the mass transfer, only occurred in refined cells. The number of refined cells on either side of the interface is referred to as δ_M, the refinement level is referred to as δ_L, and the refinement frequency is referred to as δ_T. The refinement level is the number of times each bulk cell is required to be refined before the elements within it are the same size as the cells at the interface. This refinement is displayed in Figure 3-6.

Before Refinement   After Refinement
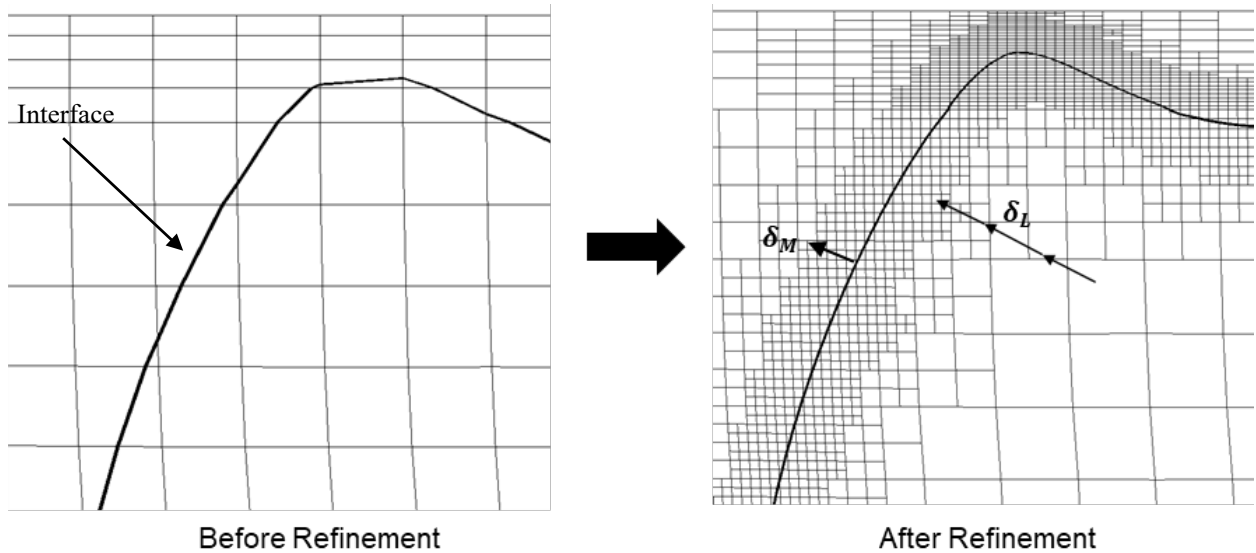
Figure 11: Mesh refinement demonstration

The extent to which the cell count could be reduced without significantly negatively affecting the solution was the primary focus of this investigation, and several benchmark tests were conducted to gauge this effect. The refinement model could be implemented in various ways. Therefore, the accuracy had to be evaluated through benchmark tests. The three major variables for the refinement model were as follows: the level at which the cells were refined, the size of the area within which the cells were refined, and the number of time steps that occurred between each refinement.

4.2. Refinement level

The level at which the cells could be refined was investigated through four tests. The first case was at $\delta_L = 0$ (all the cells being the same size), and the other cases were conducted with $\delta_L = 1$, 2 and 3 respectively. The area of refinement was set to $\delta_M = 4$ and $\delta_T = 5$, which would both be verified in the tests. The resulting HTC of the heated surface at the end of the simulation and the location of the bubble throughout the simulation were used to evaluate the influence of the variables. Figure 12 illustrates the HTC at different levels of refinement.

Figure 12 shows that the HTC only differed slightly as the level of refinement was increased, with the maximum difference being 5.3% between $\delta_L = 1$ and $\delta_L = 3$. The difference between these cases was due to the way in which the inflation layer affected the mesh generation. Cases with $\delta_L = 1$ and $\delta_L = 2$ had to have

their meshes recreated due to a conflict between refinement and the inflation layers, which required either smaller cells for a constant growth rate or for a slower growth rate. The second option was selected, which led to a less smooth transition and fewer minimum-sized elements, resulting in an overestimation of the HTC.
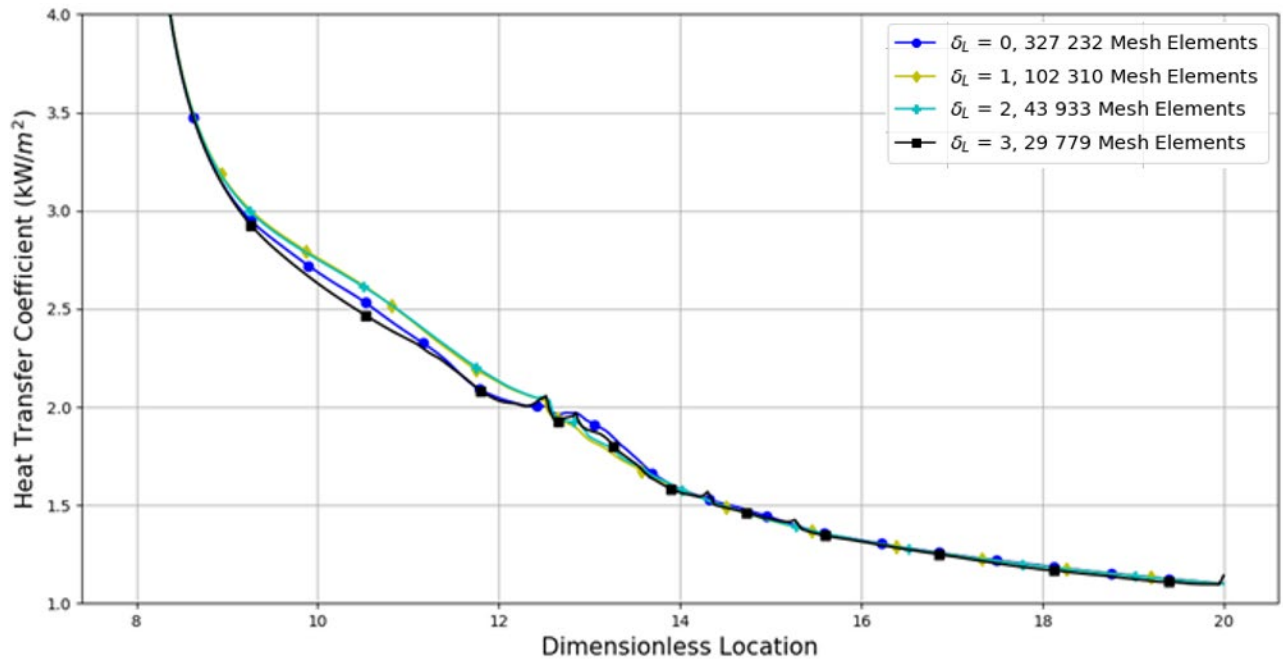

Figure 12: Heat transfer coefficient along the heated length for different mesh refinement levels

The temporal position of the slugs showed a similar trend. Figure 13 displays the position of the ends of the slug versus time for each refinement level. Here, the maximum difference between $\delta_L = 0$ and $\delta_L = 3$ was only 2%, indicating that the solution was not considerably altered by the coarser cells in the bulk flow.
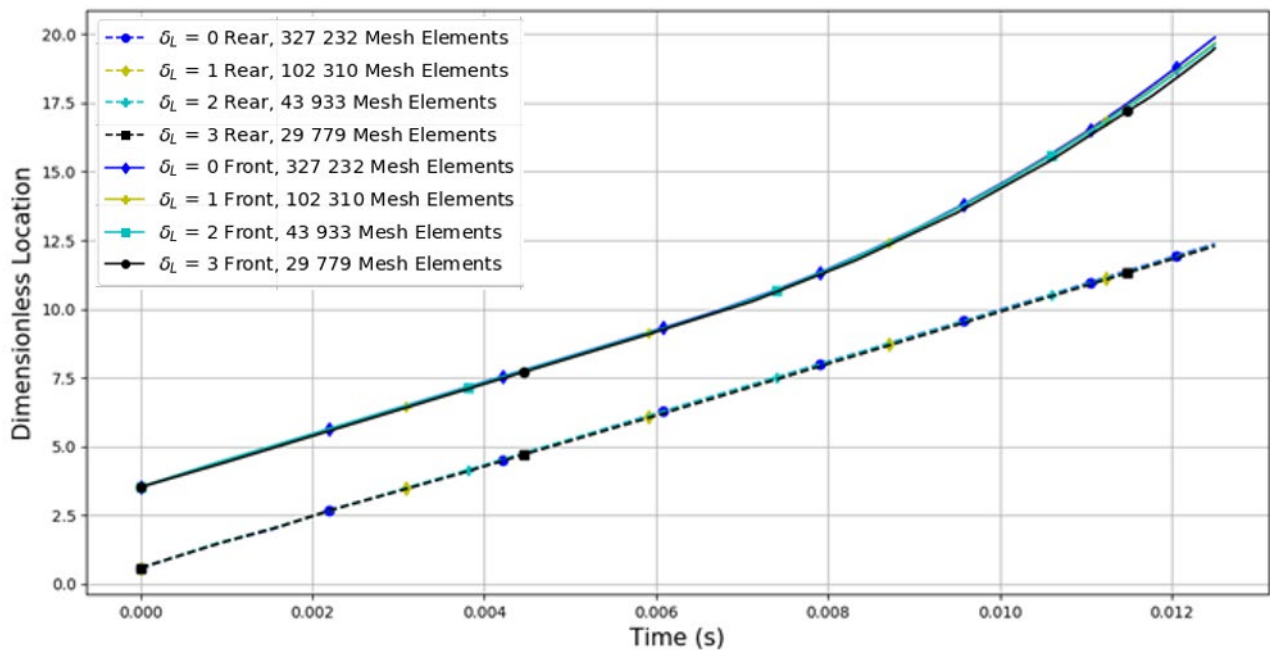
Figure 13: Dimensionless location versus time for different mesh refinement levels

4.3. Refinement area

The number of elements on either side of the interface that were necessary to capture the spurious currents and the mass transfer accurately was investigated next. This was done through four tests, the first with only the elements in the interface being refined ($\delta_M = 0$). The other tests were done with $\delta_M = 2$, 4 and 6. The cases were first evaluated with the HTC along the heated wall, shown in Figure 4. There was a very small error for the cases with $\delta_M = 4$ and $\delta_M = 6$. As the number of elements was decreased to $\delta_M = 2$ and $\delta_M = 0$, the HTC increased and became erratic, with $\delta_M = 0$ differing greatly from the rest.
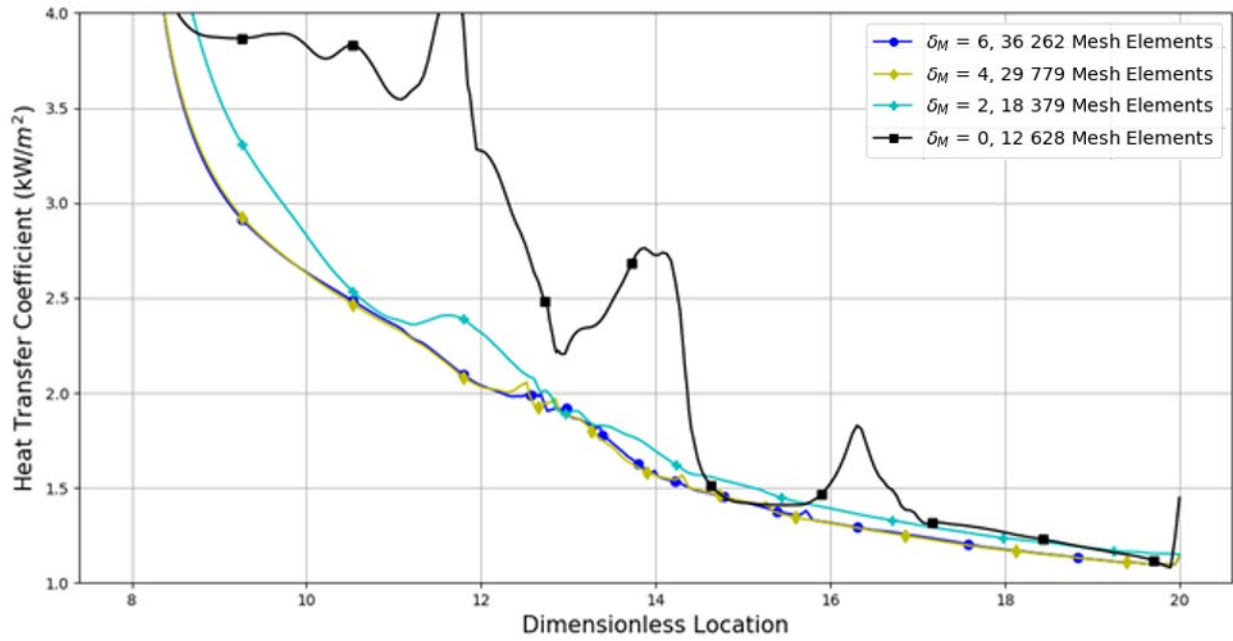
Figure 14: Heat transfer coefficient along the heated surface for different mesh refinement areas

Figure 5 indicates that the case of $\delta_M = 2$ behaved differently, with the differences in the bubble position for the last three cases being negligible. The case of $\delta_M = 0$ differed considerably as the rear of the bubble fell behind and the front exited the domain at 11.5 ms. These inconsistencies were a result of the interface constantly leaving the refinement zone. This led to a loss of information because the interface moved into larger cells. The loss continued with the refinement of the larger cells. When the mass transfer occurred in the larger cells, it led to an overestimation of the magnitude and resulted in an overestimation of the HTC.
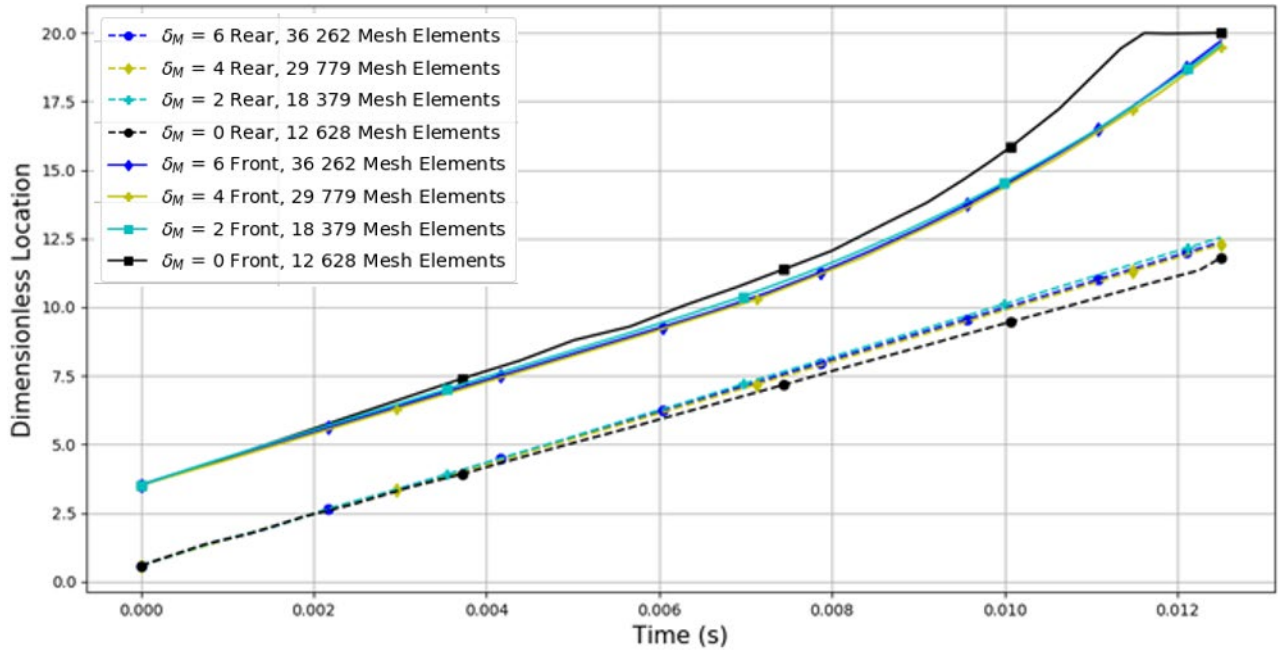
Figure 15: Dimensionless location versus time for different mesh refinement areas

The inconsistency of the refinement on the interface also led to errors with the surface tension, resulting in interesting behaviour. Figure 16 illustrates the bubble profiles just after entering and at the end of the heated section. Figure 16 indicates that the profile for the $\delta_M = 0$ case differed significantly from that of the other cases.
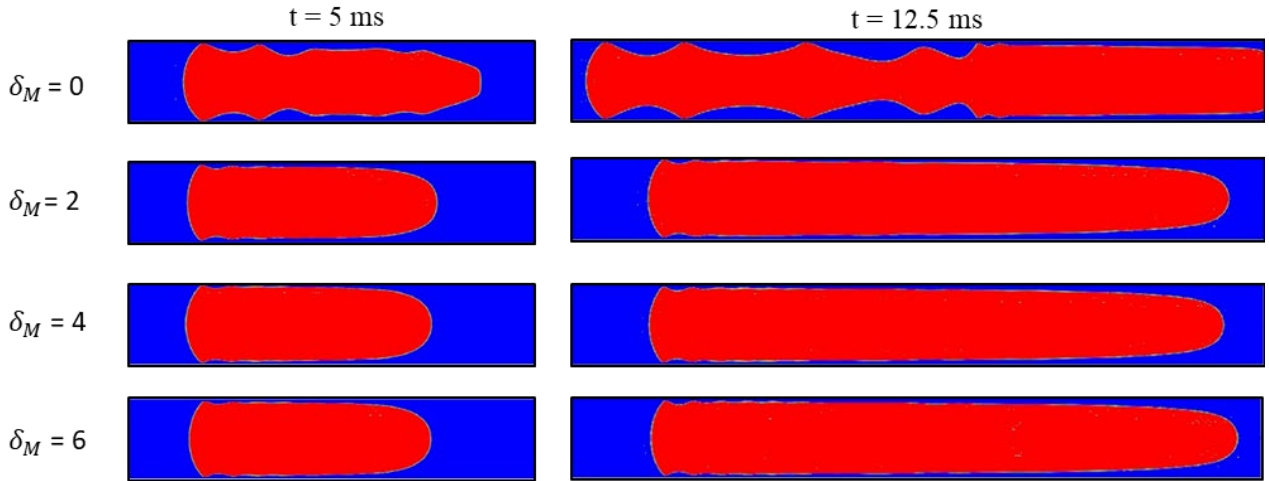

Figure 16: Bubble profiles at t = 5 ms (left) and t = 12.5 ms (right) for the zero-cell case, the two-cell case, the four-cell case and the six-cell case

Figure 14 and Figure 15 show that with reduced cell density in the bulk regions, the refinement model could still maintain accuracy as long as sufficient cells on either side of the interface were refined. The number of elements in the domain at the beginning and end of the test is listed in Table 2. The case that performed the best in terms of the minimum number of elements without sacrificing accuracy had three

levels of refinement ($\delta_L = 3$), four cells on either side of the interface ($\delta_M = 4$) and refinement occurring every five time steps ($\delta_T = 5$). This case produced similar results with 9% of the cells when compared with the base case ($\delta_L = 0$). In other words, the required computational efforts (the required number of elements) of this study is only 8.2% of that used by Magnini et al. [5] and 3.3% of Ferrari et al. [6], with negligible resulting errors.

Table 3: Number of cells for each mesh refinement benchmark test.

δ_T	δ_M	δ_L	Initial number of cells	Final number of cells
5	4	0	327 232	327 232
5	4	1	92 338	102 310
5	4	2	31 513	43 933
5	4	3	17 578	29 779
5	0	3	8 665	12 628
5	2	3	12 130	18 379
5	4	3	17 578	29 779
5	6	3	21 613	36 262

4.4. Refinement frequency

The last set of simulations was an investigation into the effect of the frequency of refinement on the solution. Indeed, in this step, the study focused on how long a simulation could carry on with the previous mesh adaptation settings before the next arrangement for refinement took place. Four cases were run, each one with an increasing number of time steps occurring before refinement took place. The meshes were refined at intervals of $\delta_T = 5, 10, 20$ and 50 time steps.
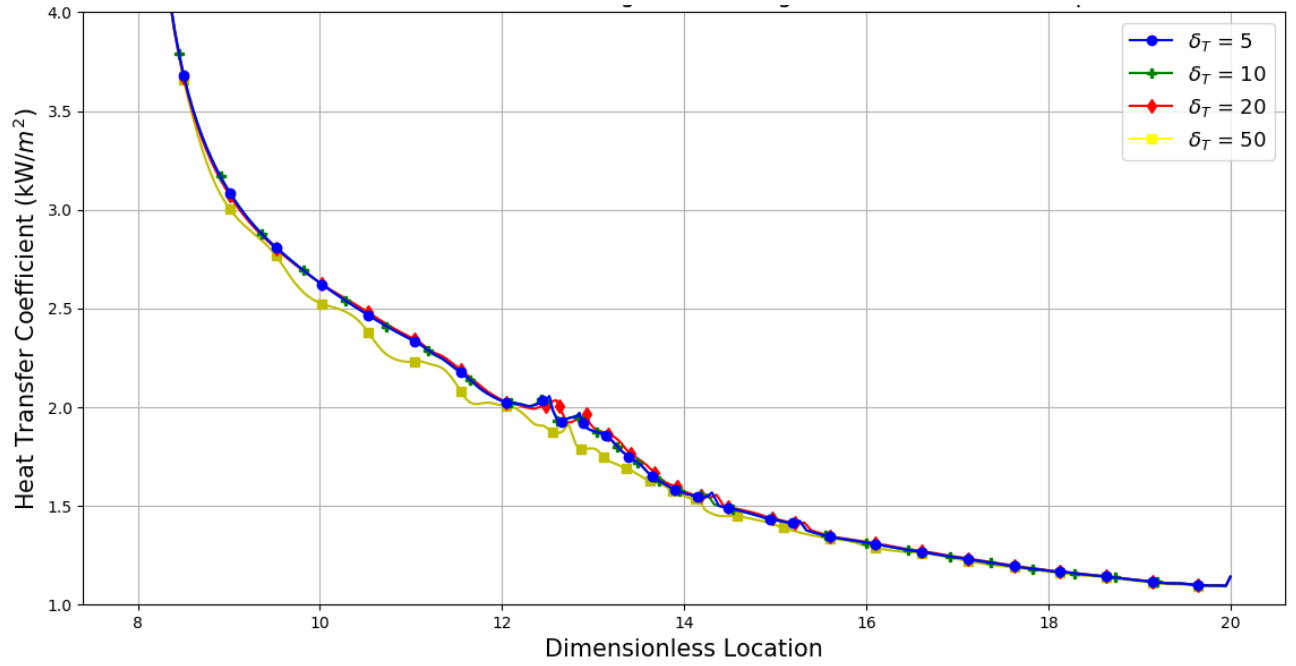
Figure 17: Heat transfer coefficient for different adaption frequencies

The adaption method operated identically when conducting the refinement at both $\delta_T = 5$ and $\delta_T = 10$, as displayed by the HTC shown in Figure 17, with the HTCs of the respective cases overlapping with no visible error. However, once the refinement frequency was increased, some error was introduced into the solution, with the HTC being slightly higher at $\delta_T = 20$ and much lower and more erratic at $\delta_T = 50$.
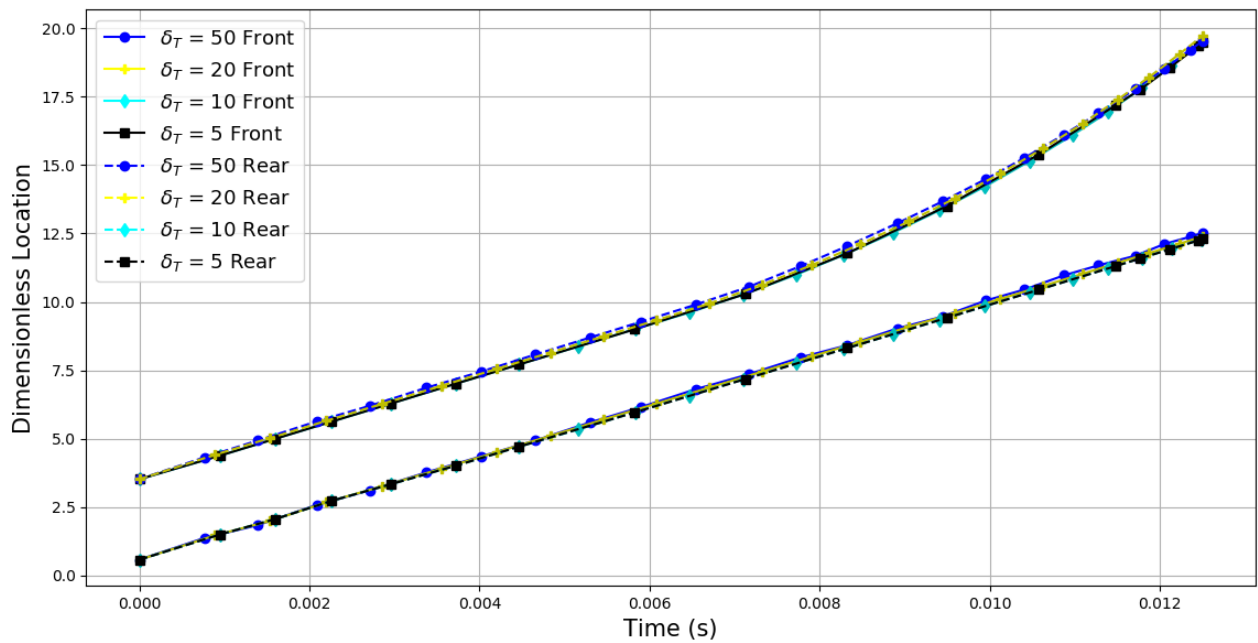

Figure 18: Dimensionless bubble positions for different adaption frequencies

The trends shown in Figure 18 were similar to those shown in Figure 17. The bubble locations of $\delta_T = 5$ and $\delta_T = 10$ were identical, while the case with $\delta_T = 20$ slightly overestimated both the rear and the front of the bubble. The $\delta_T = 50$ case varied slightly, with the rear of the bubble oscillating between being overestimated and underestimated, while the front of the bubble was overestimated throughout. The major effect of the high refinement frequency is shown in Figure 19. Because the flow direction was parallel to the heated surface, the effect of the high refinement frequency was not as noticeable. However, the areas of the bubble, which had a curvature that was parallel to the flow direction, flowed out of the refined area before the refinement method was implemented. This caused the effect of surface tension to become erratic, with the rear of the bubble oscillating between being a correctly curved surface, a pointed surface and a flat surface.

t = 7.3 ms

t = 9 ms

t = 10.4 ms

t = 11.7 ms

t = 12.5 ms

Figure 19: Bubble profiles ranging from 7.3 ms to 12.5 ms for cases with $\delta_T = 50$

The results shown in Figure 17, Figure 18 and Figure 19 indicate that the refinement method operated correctly when the refinement frequency was set to $\delta_T = 5$ or $\delta_T = 10$; however, the method started to introduce errors when it was increased due to the tendency of the bubble interface to leave and re-enter the refined area.

5. Case study

After investigating the features of the adaptive mesh approach, this approach was tested in a practical 3D multiphase case study to see how effectively it could capture the results of the study. Therefore, this section presents a short case study investigating the effect of inclination on the phase change behaviour in a square microchannel. The case study consisted of a 3D domain, and the geometry is defined in Figure 20.
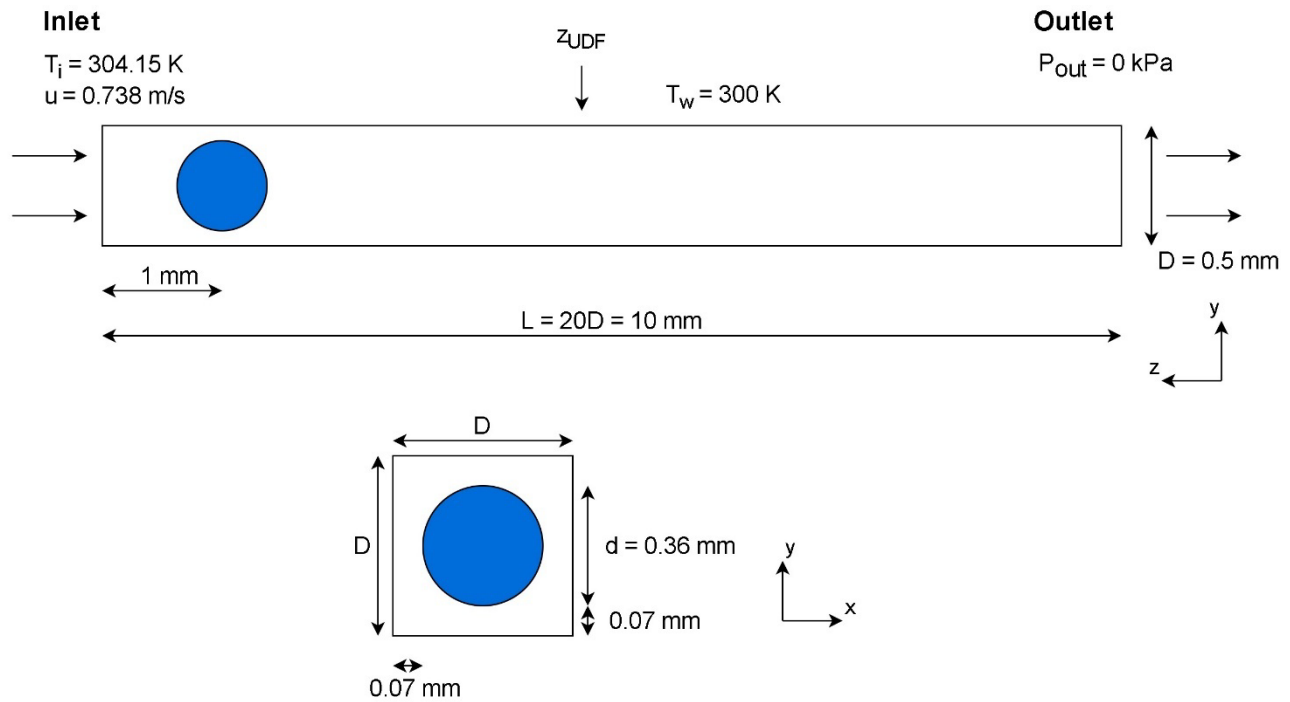
Figure 20: Side view (z-y plane) and front view (y-x plane) of the initial R245fa bubble position in the microchannel

The inclination of the channel was set by controlling the gravitational vector coordinates in Fluent. Six inclinations between 0° and 90° (to the horizontal) were used to investigate the microchannel phase change behaviour, and their components are shown in Table 4.

Table 4: Components of gravitational field strength for different channel inclinations.

Channel inclination angle [°]	x-component of gravity [m/s²]	y- component of gravity [m/s²]	z- component of gravity [m/s²]
0	0.000	-9.807	0.000
18	0.000	-9.327	3.030
36	0.000	-7.934	5.764
54	0.000	-5.764	7.934
72	0.000	-3.030	9.327
90	0.000	0.000	9.807

The working fluid in the case study simulations was refrigerant R245fa. An initially spherical R245fa vapour bubble (of radius 0.18mm) was simulated in a 0.5 mm square microchannel of length 10mm. The

boundary conditions were an inlet R245fa liquid velocity of 0.74 m/s ($Re = 1300$), a zero-gauge pressure outlet and a wall temperature of 300 K. However, the wall temperature was lower than the saturation temperature of R245fa (304.15 K), resulting in condensation rather than evaporation present in the simulations. The default wall adhesion settings were applied, and the contact angle was kept to the default 90°. Furthermore, approximately halfway into the simulation, a UDF was activated to model the phase change (and resulting mass transfer) behaviour. This position is indicated as z_{UDF} in Figure 20.

The different working fluid and boundary conditions of the case study illustrate that the adaptive mesh refinement model discussed above is not limited to a single fluid nor specific conditions. The case study simulations were used to develop a methodology for virtual reality (VR) presentation of two-phase flow. To accelerate the development process and improve the VR feasibility, a spherical bubble and a coarser mesh were used to reduce the node count.

An example of a single set of transient data for a channel inclination of $54°$ is shown in Figure 21 for a central phase contour splice in the y-z plane.
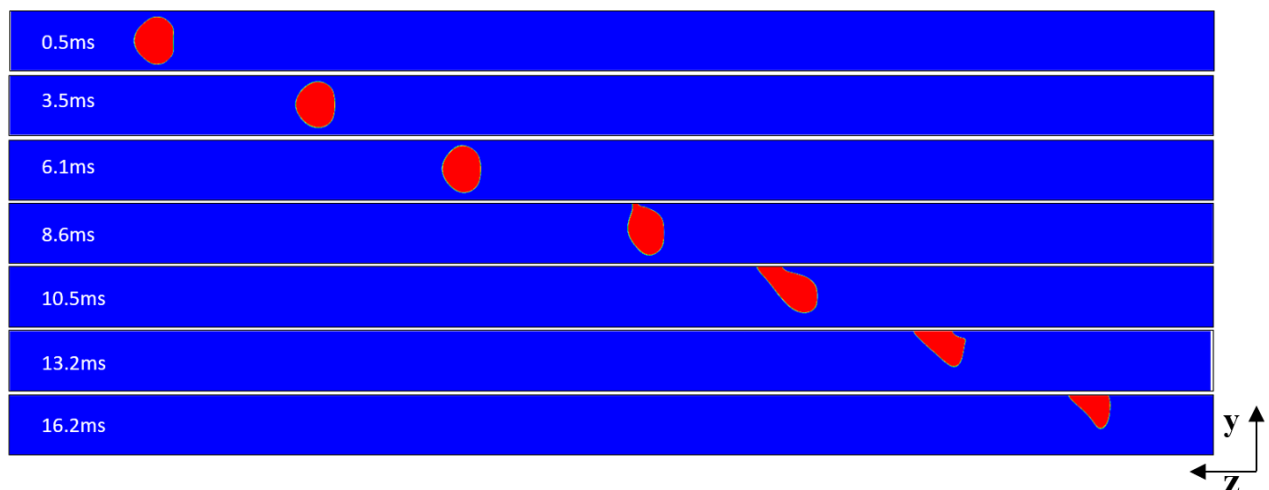

Figure 21: Eulerian frame of reference for microchannel simulation. Viewed on central y-z cross-section of vapour volume fraction and with the inlet flow on the left-hand side (blue = R245fa liquid phase and red = R245fa vapour phase)

At 0.5 ms, the bubble was warped slightly from its initial spherical shape as the (left-to-right) flowing R245fa liquid caused the interface to deform in the direction of flow. The bubble continued to move along the channel like this until 8.6 ms, where it bound to the top wall of the microchannel. By 10.5 ms, the bubble was more strongly bound to the top wall because its interface with the wall (represented by the flat line at the top of the bubble in Figure 21) was larger. This trend continued and can be seen at a time of 16.2 ms as the bubble moved towards the channel exit.

Figure 22, shows a summary of simulations for varying channel inclinations in matrix form. The vapour bubble (in red) is tracked in a Lagrangian reference frame along the channel length. The x-axis of the matrix

is simulation flow time, and the y-axis is the channel inclination angle. Bubble shapes are from a central cross-section through the channel on a z-y plane, and the sections which display a flat horizontal line are in contact with the channel walls, at the line.
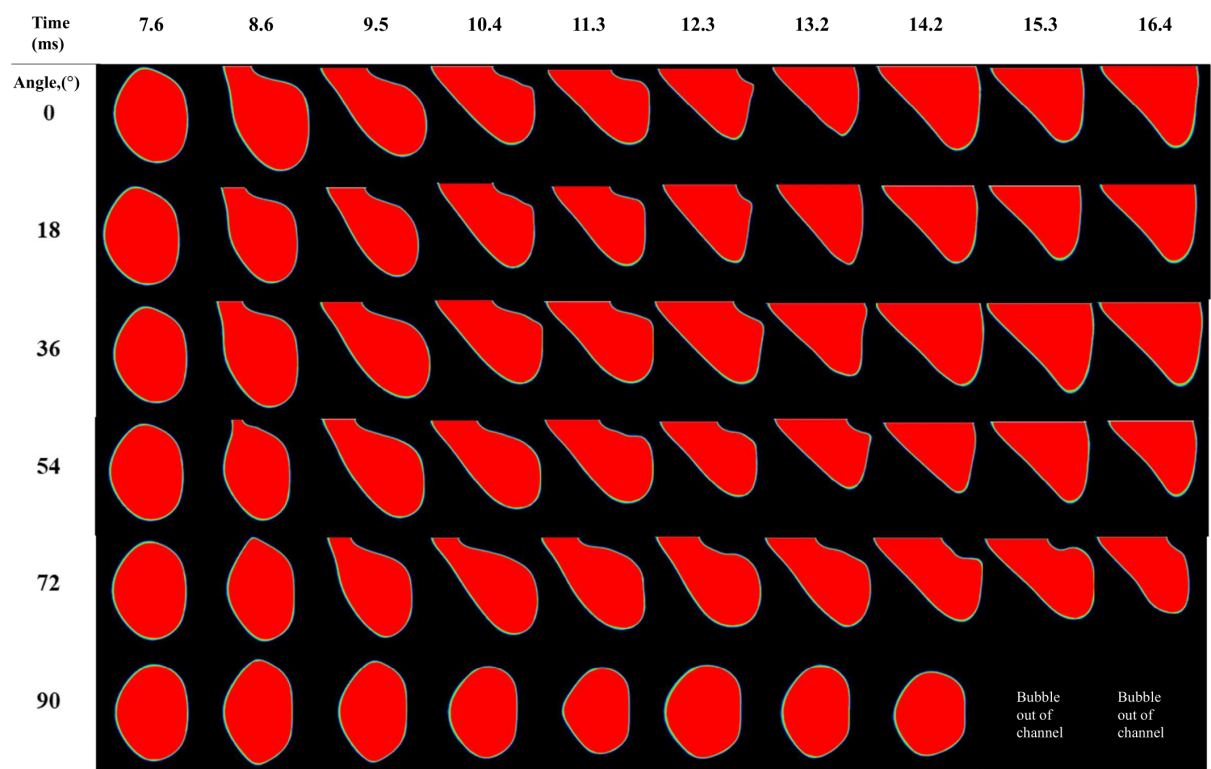

Figure 22: R245fa vapour bubble (at + a central cross-section in the z-y plane) with varying simulation time for six inclinations (straight line interface of bubble caused by contact with channel wall)

For a horizontal run (0°), the bubble attached to the top wall by 8.6 ms, and the interfacial area in contact with the wall clearly increased as the simulation proceeded, which is illustrated in Figure 22 by the horizontal line representing the contact with the wall. This trend is observed on all simulation runs bar the vertical (90°) run and is analysed numerically in more detail (for 0° to 54°) in the following section. As the channel inclination increased up to 72 degrees, the level of bubble attachment to the top wall clearly decreased. Comparing (10.4 ms, 0 degrees) with (10.4 ms, 72 degrees), the bubble in the more inclined channel is observed to be scarcely in contact with the top wall in contrast to the horizontal channel. The leading bubble edge for lower inclinations can also be observed to flatten out sooner than for higher inclinations, maintaining a leading edge, which dragged on the top wall. See the time frame for 13.2 ms.

The change in bubble volume with respect to simulation time was investigated. The results were extracted and processed from the large Fluent output files via a Python script developed by the authors.
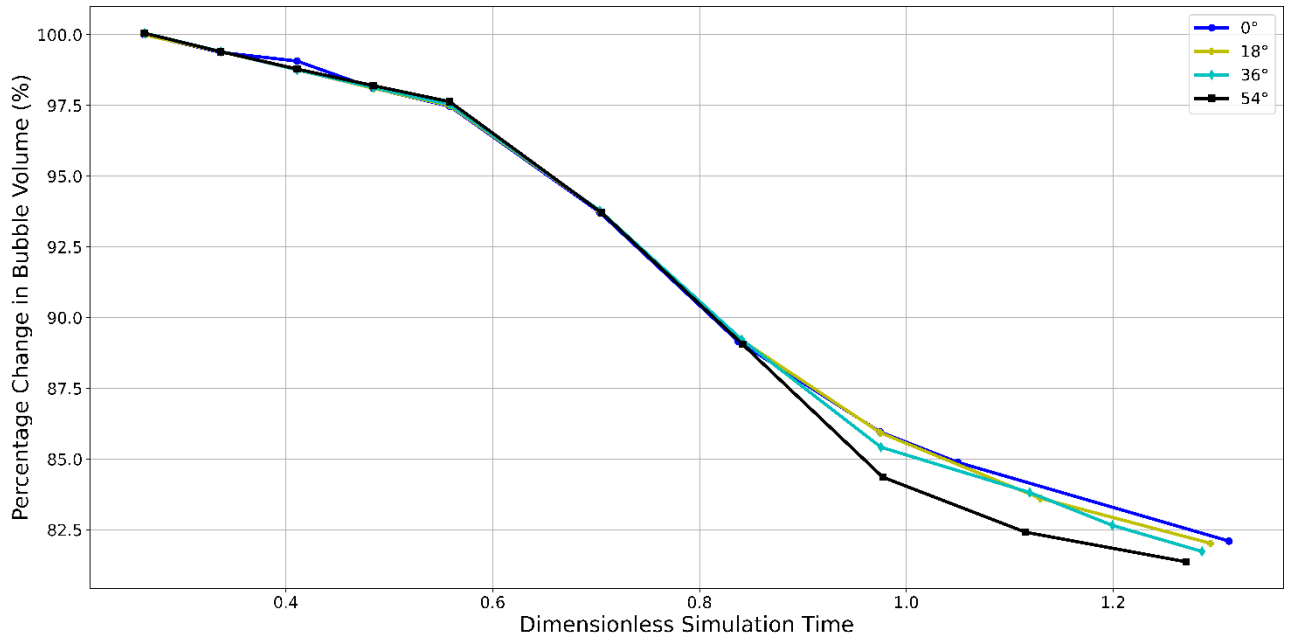
Figure 23: Bubble volume change with respect to dimensionless simulation time due to condensation (dimensionless simulation time determined via channel residence time)

The bubble volume is noted to decrease throughout the simulation, by 18 to 19% for all simulation runs shown. The y-axis shows the volume of the bubble as a percentage of the original volume, and the x-axis shows the dimensionless simulation time, t_d. This was calculated with reference to the channel residence time. All bubbles show similar shrinking rates up until a dimensionless simulation time of ≈ 0.85, apart from a minor fluctuation in the horizontal case at ≈ 0.40. After this time, the bubble shrinking rates began to vary slightly with some crossover between the 18° and 36° inclination behaviours. Results of inclinations of 72° and 90° could be analysed in further research, but more time on the cluster computing system would be required to achieve this.

It was also considered that the interfacial area of the bubble in contact with the microchannel walls would give a good indication of the heat transfer behaviour taking place. As in the case of the bubble shrinking rate data extraction, a Python script was developed to determine the interfacial wall contact area.
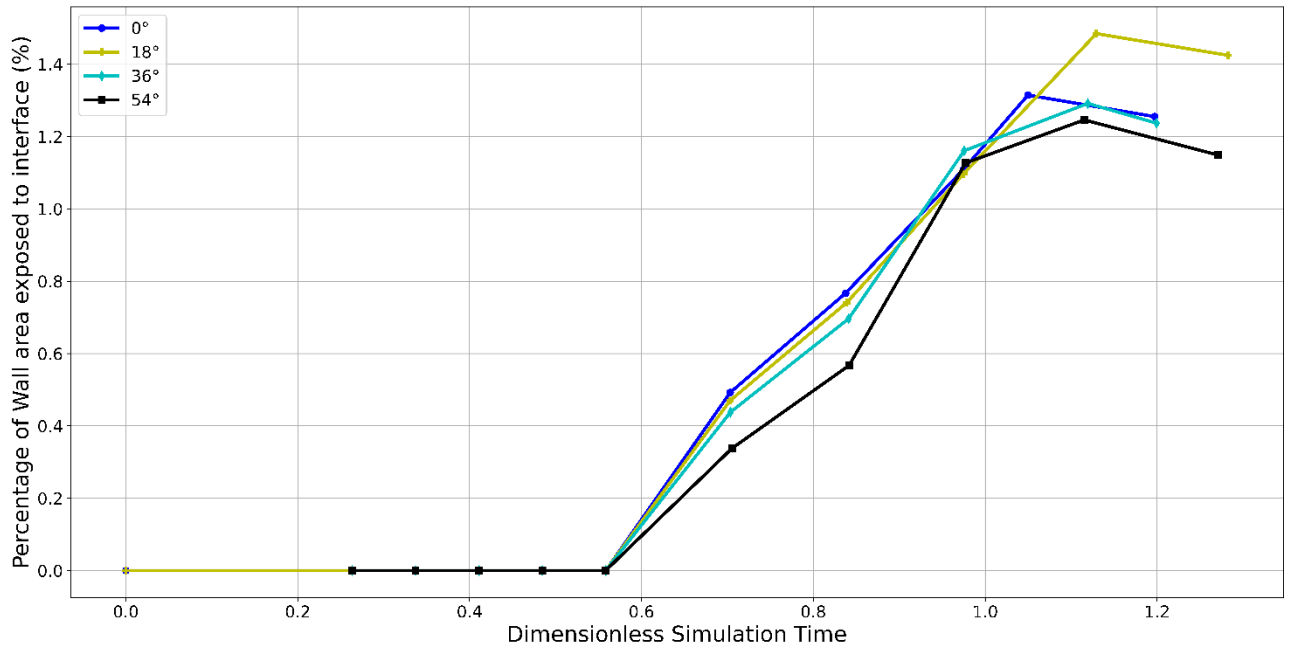
Figure 24: Bubble interfacial area in contact with walls as simulation progresses (dimensionless simulation time determined via channel residence time)

Figure 24 shows that between a dimensionless simulation time of ≈ 0.55 and ≈ 0.70, the bubble contacts the microchannel walls. The figure also shows that the bubble has not yet contacted the walls at $t_d \approx 0.55$ because the percentage of wall area exposed to the interface is 0. As the simulation progresses, the channel inclination is shown to affect the interfacial contact area significantly. The more inclined simulation runs are shown to contact the channel walls less than the horizontal case for the same simulation time. This statement is only true until $t_d \approx 0.98$ where all cases show similar wall contacting. As the simulation progresses, the contact area for the 18° inclined channel is observed to show the greatest interfacial contact area with the walls. The 18° run shows an approximately 25% increase from the 54° run for peak interfacial area contact. This increase suggests that the highest heat transfer rates may be observed for this inclination. For $t_d > 0.98$, the interfacial areas fluctuate significantly, showing peak contact areas at varying times for each inclination. Although the data is coarse, Figure 24 indicates that the peak areas (as percentages of the total channel area) for the 0°, 18°, 36° and 54° runs are 1.29%, 1.48%, 1.29% and 1.12% respectively.

The final dataset to discuss is that of the local heat transfer coefficient calculated by Equation 18. This was determined with respect to the "wall adjacent temperature" variable in ANSYS Fluent. Figure 25 shows an example contour set of the local heat transfer coefficient taken in the boundary layer of the top wall (at $y = 0.499mm$) for a channel inclination of 54° at 0.015 s.
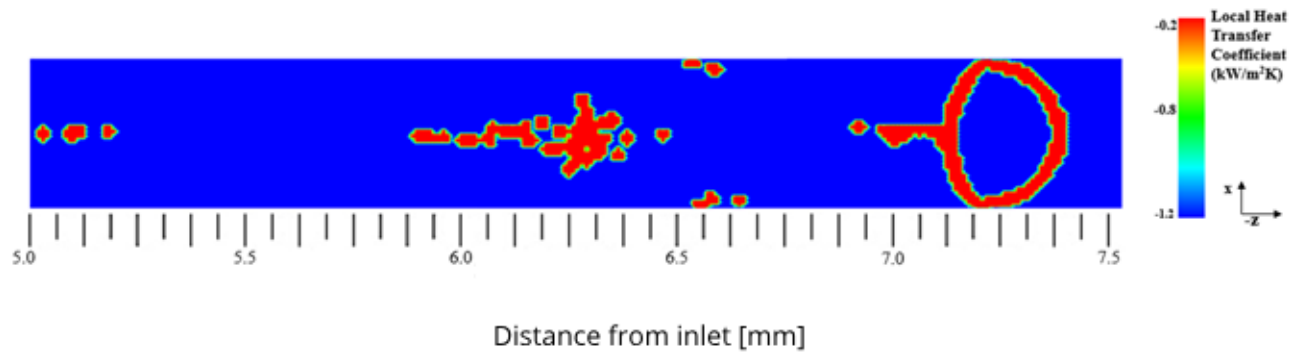
Distance from inlet [mm]

Figure 25: Contours of local heat transfer coefficient for a channel inclination of 54 degrees at 0.015 seconds (taken on a plane in the x-z direction at a y coordinate of 0.499 mm)

The negative heat transfer coefficients obtained suggest that condensation behaviour occurred and that heat was transferred from the bubble to the microchannel wall. The red contour corresponds to a temperature of 279.15 K, and the blue contour to a temperature of 300.00 K. On the red contour, the lower temperature indicates a condensation phase change taking place. Figure 25 shows the presence of a condensing vaporous trail that follows the bubble as it moves in the z-direction.

6. Conclusion

An extensive review of the numerical simulation of flow boiling in microchannels highlighted the many limitations that exist. The incredibly small scales that are involved in the process require tiny computational cells, which induce incredibly high computational costs. To decrease the number of cells required to capture the small-scale phenomena under investigation accurately, an interface-tracking adaptive mesh refinement model was proposed. The model was used to recreate two previously published studies. Several benchmark tests were conducted to investigate how many levels of refinement could be implemented, how many cells were required around the interface and how often the refinement method had to occur. The accuracy of the simulation was analysed as the cell count was reduced, resulting in a mesh that produced results comparable with previously published studies. The final mesh refinement model had three levels of refinement (δ_L = 3), four refined cells on either side of the interface (δ_M = 4) and was implemented every five time steps (δ_T = 5). The maximum error between the results of this study and those of Ferrari et al. [6] was 6.7%, while about 1.6% of the cells were used.

The effectiveness of this method was illustrated through a case study. The case study also showed that the model could be used for both evaporation and condensation. This study paves the way for further research to obtain the results of flow boiling with maximum accuracy and minimum computational effort, which would allow researchers to run 3D simulations of flow boiling and expedite their research process in properly capturing the flow-boiling features.

7. Acknowledgements

8. References

1. A. Bordbar, A. Taassob, A. Zarnaghsh and R. Kamali, Slug flow in microchannels: Numerical simulation and applications, Journal of industrial and engineering chemistry 62 (2018) 26-39.

2. A.R. Betz and D. Attinger, Can segmented flow enhance heat transfer in microchannel heat sinks?, International Journal of Heat and Mass Transfer 53 (19) (2010) 3683-3691.

3. M. Magnini and J. Thome, A CFD study of the parameters influencing heat transfer in microchannel slug flow boiling, International Journal of Thermal Sciences 110 (2016) 119-136.

4. S. Szczukiewicz, M. Magnini and J.R. Thome, Proposed models, ongoing experiments, and latest numerical simulations of microchannel two-phase flow boiling, International journal of multiphase flow 59 (2014) 84-101.

5. M. Magnini, B. Pulvirenti and J.R. Thome, Numerical investigation of hydrodynamics and heat transfer of elongated bubbles during flow boiling in a microchannel, International Journal of Heat and Mass Transfer 59 (2013) 451-471.

6. A. Ferrari, M. Magnini and J.R. Thome, Numerical analysis of slug flow boiling in square microchannels, International Journal of Heat and Mass Transfer 123 (2018) 928-944.

7. Y.Q. Zu, Y.Y. Yan, S. Gedupudi, T.G. Karayiannis and D.B.R. Kenning, Confined bubble growth during flow boiling in a mini-/micro-channel of rectangular cross-section part II: Approximate 3-D numerical simulation, International Journal of Thermal Sciences 50 (3) (2011) 267-273.

8. M. Magnini, B. Pulvirenti and J. Thome, Numerical investigation of the influence of leading and sequential bubbles on slug flow boiling within a microchannel, International Journal of Thermal Sciences 71 (2013) 36-52.

9. R. Gupta, D.F. Fletcher and B.S. Haynes, On the CFD modelling of Taylor flow in microchannels, Chemical Engineering Science 64 (12) (2009) 2941-2950.

10. D. Liu, X. Ling, H. Peng, J. Li and L. Duan, Experimental and numerical analysis on heat transfer performance of slug flow in rectangular microchannel, International Journal of Heat and Mass Transfer 147 (2020) 118963.

11. J.R. Thome, Boiling in microchannels: a review of experiment and theory, International Journal of Heat and Fluid Flow 25 (2) (2004) 128-139.

12. A. Mehdizadeh, S.A. Sherif and W.E. Lear, Numerical simulation of thermofluid characteristics of two-phase slug flow in microchannels, International Journal of Heat and Mass Transfer 54 (15) (2011) 3457-3465.

13. T. Fondelli, A. Andreini and B. Facchini, Numerical Simulation of Dam-Break Problem Using an Adaptive Meshing Approach, Energy Procedia 82 (2015) 309-315.

14. C.H. Zhou and J.Q. Ai, Mesh adaptation for simulation of unsteady flow with moving immersed boundaries, International Journal for Numerical Methods in Fluids 72 (4) (2013) 453-477.

15. M. Bayareh, M. Nasr Esfahany, N. Afshar and M. Bastegani, Numerical study of slug flow heat transfer in microchannels, International Journal of Thermal Sciences 147 (2020) 106118.

16. A. Ma, J. Wei, M. Yuan and J. Fang, Enhanced flow boiling heat transfer of FC-72 on micro-pin-finned surfaces, International Journal of Heat and Mass Transfer 52 (13) (2009) 2925-2931.

17. M. Law and P.-S. Lee, A comparative study of experimental flow boiling heat transfer and pressure characteristics in straight- and oblique-finned microchannels, International Journal of Heat and Mass Transfer 85 (2015) 797-810.

18. W. Wan, D. Deng, Q. Huang, T. Zeng and Y. Huang, Experimental study and optimization of pin fin shapes in flow boiling of micro pin fin heat sinks, Applied Thermal Engineering 114 (2017) 436-449.

19. R. Ajith Krishnan, K.R. Balasubramanian and S. Suresh, The effect of heating area orientation on flow boiling performance in microchannels heat sink under subcooled condition, International Journal of Heat and Mass Transfer 110 (2017) 276-293.

20. M. Vermaak, J. Potgieter, J. Dirker, M.A. Moghimi, P. Valluri, K. Sefiane, and J.P. Meyer, Experimental and numerical investigation of micro/mini channel flow-boiling heat transfer with non-uniform circumferential heat fluxes at different rotational orientations, International Journal of Heat and Mass Transfer 158 (2020) 119948.

21. K.R. Balasubramanian, R.A. Krishnan and S. Suresh, Spatial orientation effects on flow boiling performances in open microchannels heat sink configuration under a wide range of mass fluxes, Experimental Thermal and Fluid Science 99 (2018) 392-406.

22. W. Li, Z. Chen, J. Li, K. Sheng and J. Zhu, Subcooled flow boiling on hydrophilic and super-hydrophilic surfaces in microchannel under different orientations, International Journal of Heat and Mass Transfer 129 (2019) 635-649.

23. R. Courant, K. Friedrichs and H. Lewy, On the partial difference equations of mathematical physics, IBM journal of Research and Development 11 (2) (1967) 215-234.

24. Q. Liu and B. Palm, Numerical study of bubbles rising and merging during convective boiling in micro-channels, Applied Thermal Engineering 99 (2016) 1141-1151.

25. R.W. Schrage, A Theoretical Study of Interphase Mass Transfer, Columbia University Press, 1953.

26. I. Tanasawa, Advances in Condensation Heat Transfer. in: J.P. Hartnett, T.F. Irvine, and Y.I. Cho, eds, Advances in Heat Transfer, Elsevier, Tokyo, 1991, pp. 55-139.

27. S. Hardt and F. Wondra, Evaporation model for interfacial flows based on a continuum-field representation of the source terms, Journal of Computational Physics 227 (11) (2008) 5871-5895.

28. C.R. Kharangate and I. Mudawar, Review of computational studies on boiling and condensation, International Journal of Heat and Mass Transfer 108 (2017) 1164-1196.

Declaration of interests

☒ The authors declare that they have no known competing financial interests or personal relationships that could have appeared to influence the work reported in this paper.

☐The authors declare the following financial interests/personal relationships which may be considered as potential competing interests: